Estimation of Phytoplankton Chlorophyll-a Concentration in the Western Basin of Lake Erie Using Sentinel-2 and Sentinel-3 Data

by

Somayeh Mollaee

A thesis
presented to the University of Waterloo
in fulfillment of the
thesis requirement for the degree of
Master of Science
in
Geography

Waterloo, Ontario, Canada, 2018

Author's Declaration

I hereby declare that I am the sole author of this thesis. This is a true copy of the thesis, including any required final revisions, as accepted by my examiners.

I understand that my thesis may be made electronically available to the public.

Abstract

Worldwide phenomena called algae bloom has been recently a serious matter for inland water bodies. Temporal and spatial variability of the bloom makes it difficult to use in-situ monitoring of the lakes. This study aimed to evaluate the potential of Sentinel-3 Ocean and Land Colour Instrument (OLCI) and Sentinel-2 Multispectral Instrument (MSI) data for monitoring algal blooms in Lake Erie. Chlorophyll-a (Chl-a) related products were tested using NOAA-Great Lakes Chl-a monitoring data over summer 2016 and 2017. Thematic water processor, fluorescence line height/maximum chlorophyll index (MCI) and S2 MCI, plug-in SNAP were assessed for their ability to estimate Chl-a concentration. We processed both Top of the Atmosphere (TOA) reflectance and radiance data.

Results show that while FLH algorithms are limited to lakes with Chl-a $< 8\ mg\, m{-}3$, MCI has the potential to be used effectively to monitor Chl-a concentration over Eutrophic lakes. Sentinel-3 MCI is suggested for Chl-a $> 20\ mg\, m{-}3$ and Sentinel-2 MCI for Chl-a $> 8\ mg\, m{-}3$. The different Chl-a range limitation for the MCI products can be due to the different location of the maximum peak bands, 705 and 709 for MSI and OLCI sensors respectively. TOA radiances showed a significantly better correlation with in situ data compared to TOA reflectances which may be related to the poor pixel identification during the process of pixel flagging affected by the complexity of Case-2 water. Our finding suggests that Sentinel-2 MCI achieves better performance for Chl-a retrieval ($R^2 = 0.90$). However, the FLH algorithms outperformed showing negative reflectance due to the shift of reflectance peak to longer wavelengths along with increasing Chl-a values. Although the algorithms show moderate performance for estimating Chl-a concentration, this study demonstrated that the new satellite sensors, OLCI and MSI, can play a significant role in the monitoring of algae blooms for lake Erie.

Acknowledgements

First, I would like to thank my supervisor, Professor Claude Duguay, for his financial support and advice throughout this project. I would also like to express my thanks to Professor Jonathan Li who initially gave me the opportunity to start my studies here at the University of Waterloo. Thank you to Professor Richard Kelly who has helped me to develop critical thinking skill in research, mainly through class 603. Thank you to the University Writing and Communication Centre, especially Jane Russwurm for offering all helpful feedbacks during writing this research. I also acknowledge Dr. Kiana and Dr. Homa for their valuable time to be part of my committee members. Finally, I would like to thank all my friends, officemates, and the MAD team, especially Mike Lancker, for their support over the years of doing this research.

Dedication

This thesis is dedicated to:

The people who show love to the earth and who work hard to make the world a better and safer place to live.

To my husband, Mahyar, my parents, and sibling for all their patients and motivation.

To all my teachers and people who have taught me many valuable things that have made my life more beautiful and happier.

To many women all over the world who do not have the opportunity to freely learn and do what they love.

Table of Contents

List of Tables

List of Figures

List of Abbreviations

CDOM	Colored Dissolve Organic Matters
OAC	Optically Active Constituents
RTE	Radiative Transfer Equation
NAP	Nan-Algae Particle
IOP	Inherent Optical Properties
AOP	Apparent Optical Properties
TSS	Total Suspended Sediments
NIR	Near-Infrared
OLCI	Ocean and Land Color Instrument
MERIS	Medium Resolution Imaging Spectrometer
ESA	European Space Agency
FLH	Fluorescence Line Height
MCI	Maximum Chlorophyll Index
SNR	Signal to Noise Ratio
PSI	Photosystems 1
PSII	Photosystems 2
LHC	Light Harvesting Complexes
SICF	Sun-Induced Fluorescence,
CI	Cyanobacteria Index
MPH	Maximum Peak-Height
NDCI	Normalized Difference Chlorophyll Index
ARPH	Adaptive Reflectance Peak Height Model
CZCS	Coastal Zone Color Scanner
NRT	Near-Real-Time
NTC	Non-Time Critical
TOA	top Of the Atmosphere
MSI	Multi-Spectral Instrument
SIOP	Specific Inherent Optical Properties

Chapter 1

Introduction

1.1 General introduction

Lakes offer essential ecological, environmental, hydrology and socioeconomic services. These habitats provide food supply, water supply, and have enormous biodiversity in addition to carrying out climate, hydrological, and biogeochemical regulation and pollution control. Environmental changes such as climate, land cover, and development pressure, in particular deforestation, lost vegetation cover, increased in nutrient runoff, urbanization, and watershed modification rapidly degraded water quality. These changes and pressures cause eutrophication (the excessive richness of nutrients in the water, which the water system cannot tolerate), increased turbidity, deterioration of water clarity, and loss of aquatic benthos. Moreover, they make a risk for human and animal health. Therefore, the management and monitoring of lakes should be a priority of environmental resource management which needs a low cost and effective program. To be successful in this plan, in addition to regularly ground-based monitoring methods, a cost-efficient, high spatial and temporal coverage method is a demand, and remotely sensed satellite images are a powerful tool for this.

1.2 Need for monitoring phytoplankton Chl-a

Half of the oxygen that sustains life on earth is produced by a floating plantlike organism on the surface of the ocean and inland waters, named phytoplankton. They are the most primary producer of the food web in the aquatic systems due to their ability to photosynthesise, a process of making organic compounds using dissolved carbon dioxide and sunlight energy. Therefore, phytoplankton are the agent of primary production in the lakes while sustaining the food cycle in the water. Because of this, phytoplankton are interesting to researchers to assess biogeochemical cycles. However, in inland waters, monitoring and research programs on phytoplankton are less focused on the biogeochemical application; in fact, they are more concerned with controlling interventions. Having said that, the pressure of human impact, mainly eutrophication and climate change, has a severe influence on phytoplankton's natural balance and can cause a phenomenon named bloom. Bloom is an increase in population and reproducing of the phytoplankton species in an excessive growth. Blooms can effect water quality and cause loss of aquatic biodiversity. One type of phytoplankton, cyanobacteria, may produce a deadly toxin which is a risk to human and animal health. In general two main classes of phytoplankton are algae and cyanobacteria. Diatoms, dinoflagellates, green algae, cyanobacteria, and coccolithophores are the most common types of all kinds of groups [6] (Fig. 1.1).

Algae are essential aquatic photosynthesis organisms. These are carbon fixing, oxygenating, and simple eukaryotic, single-celled or multiple cellular plants floating on the surface layer of water with a lack of stem, root, leaves or vascular system seen more in eutrophic rich-nutrient waters. Algae are difficult to classify. The various species are very different from each other. They can be grouped by their color (e.g., yellow, green, and red, brown). They are different not only based on color, but also in cellular structure and chosen environment to live. This complexity brings their taxonomy under debate. There are thousands of species of microalgae (algae) drifting within the water systems every place of the world. Figure 1.2 shows a simplified classification of this phytoplankton [6].

Algae bloom can be a significant natural phenomena in fresh waters, as a boosting factor of primary productivity. This natural occurrence may take place seasonally (e.g.,

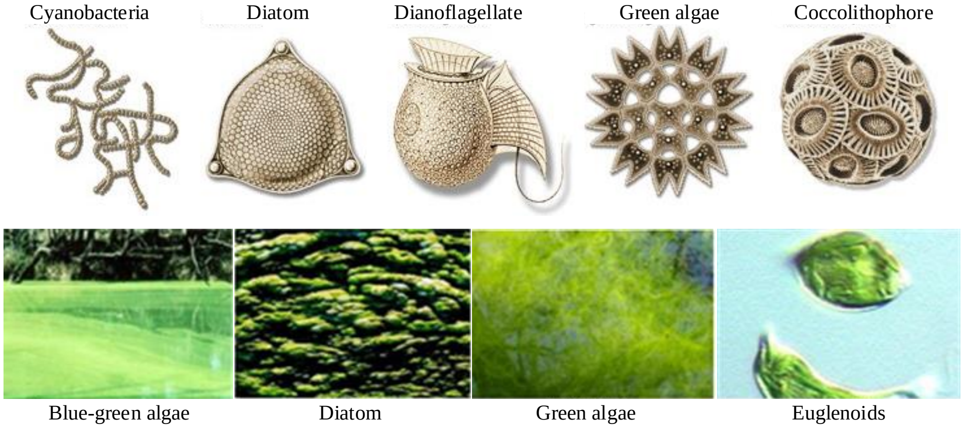

Figure 1.1: Illustrations of key inland water phytoplankton [5].

summer) due to water body characteristics and environmental conditions. The bloom commonly happens with the presence of a high level of nutrients, particularly some of the phosphates, collectively with a sunny, warm, and less windy situation or natural causes, for example a rainstorm. Although algae bloom is an important natural occurrence, in some cases, severe bloom can have critical issues for the aquatic ecosystem. For instance, when phosphates enter a water body in high-level amounts, they contribute to accelerating the growth of living biomass. The algae usually survive one week or, in favorable water conditions up to an entire summer, resulting in a massive concentration of dead organic matter which begins to decay. The decomposition needs a significant amount of dissolved oxygen and leads to severe hypoxia which threatens for fish and the aquatic animals during the summer [6].

Blue-green algae, commonly known as cyanobacteria, are bacteria (despite their ability to do photosynthesis) seen in fresh and saline waters. The name blue-green comes from the bluish color pigment, phycocyanin. The main light harvesting pigments in cyanobacteria are Phycobilipigments (phycoerythrin, phycoerythrocyanin, phycocyanin and allophycocyanin). Some of the cyanobacteria species produce a type of toxin, Cyanotoxins, accommodated in their cells. Cyanotoxins are on the Contaminant Candidate List (CCL). The most common cyanotoxins are Microcystins, cylindrospermopsin, anatoxins and sax-

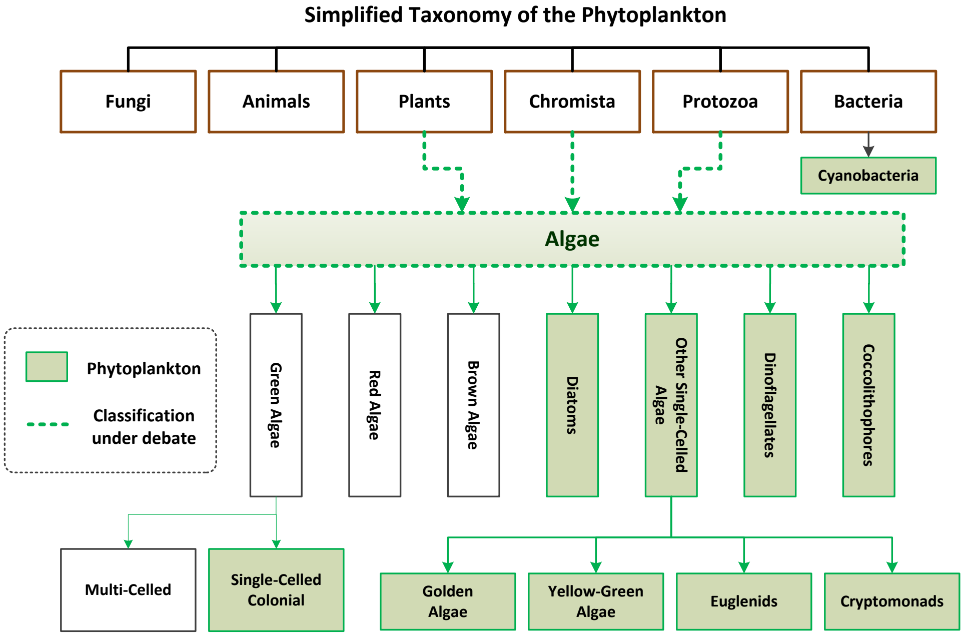

Figure 1.2: Simplified taxonomy of the phytoplankton [6].

itoxins [11]. As the most common cyanotoxins, Microcystins are generated by Anabaena, Fischerella, Gloeotrichia, Nodularia, Nostoc, Oscillatoria, Microcystis, and Planktothrix which can harm the liver, nervous system, or bioaccumulate in common aquatic species such as fish, mussels, and zooplankton [12]. Cyanotoxins can tolerate both cold and warm, even boiling water conditions. The World Health Organization (WHO) established provisional value water-quality guidelinees of 1.5 mg/L per liter for drinking water [13] and concentrations of less than 10 g/L threshold for recreational waters [14].

Chl-a pigment is present in all algae species and cyanobacteria as a primary light harvesting pigment responsible for capturing sunlight for photosynthesis along with accessory pigments such as Chl-b (650), Chl-c(630), carotenoids, phycobilins. Chl-a absorbs light highly in blue (∼440nm) and red (∼670nm). In algae, which is a eukaryotes phytoplankton, Chl-a produces in chloroplast structure, a place where photosynthesis process happens. Chloroplast contains membranes, named thylakoid, and Chl-a are embedded in this membrane. In cyanobacteria, which is a prokaryotes cell, Chl-a produces in chromatoplasm with the lack of thylakoid. Chl-a is a vital indicator of water quality as it is seen in all phytoplankton groups and is the fundamental measurement and estimating phytoplankton biomass and primary productivity for monitoring of lakes.

In sum, specific examples of damages happening by harmful algal blooms to humans and aquatic life have been very well documented by researchers, showing the necessity for prediction, early warning, and quantification of these algal blooms. Innovative technologies and methods are varying and changing for water quality monitoring. Advanced measurement technologies which assess and monitor aquatic ecosystems include modeling, portable and ground remote sensing, and satellite sensors. Knowing the trends of phytoplankton distribution and frequency and times of a bloom is one of the critical factors to protecting water resources [11].

1.3 Rational for use of remote sensing for phytoplankton Chl-a monitoring

The idea of using remote sensing for water monitoring emerged in 1960. The aim was to study ocean color with the assumption of the possibility to estimate Chl-a as a proxy of phytoplankton and sea surface temperature (SST) via a remote sensing technique [15,16]. Based on this perception, researchers started to estimate optically active constituents (OAC), such as Colored Dissolved Matters (CDOM), suspended particles, and phytoplankton remotely [17]. Subsequently the concept of ocean optics and the theory of Radiative Transfer Equation (RTE) were developed and became the basis of bio-optical modeling. Nevertheless, the application of these theories and techniques have only been used less than 30 years for inland waters, which are different compared to oceans.

Morel and Prieur [18] suggested two different classes of water: case I and case II base on the ratios of 443 and 550 nm (higher than 1.0 assumed case I and less than 1.0 case II). A newer assumption by [19] was that case I water optical properties are mainly controlled by phytoplankton where case II water is dominated by other water constituents such as CDOM and Nan-Algae Particle (NAP). However, the main criticism of this assumption is that inland water can be dominated by phytoplankton that can be assumed case I. Nevertheless, this classification is useful to having a view of two water types.

The current launch of new satellites and improvements in processer tools have significantly improved and enhanced real-time observing and the fast detection of algae blooms with improved spatial and spectral resolutions offered by the sensors and enhanced understanding of the biophysical properties of waters. Once a photon of light meets a water medium there is an interaction: the water can absorb the light and change it to heat energy, which is called the absorption coefficient or absorbance, or it partially changes the light direction, which is called scattering. The absorption and scattering properties of water are the foundation for the use of Optical Remote Sensing system (ORS) to use in measurement of water constituents. These can be expressed in terms of Inherent Optical Properties (IOPs) and Apparent Optical Properties (AOPs).

IOPs are those characteristics of the water that are independent of angular radiance distribution of the light field, and instead, rely on the water medium. Three basic IOPs related to optical remote sensing sensor are absorption coefficient, volume scattering function, and beam attenuation coefficient. In general, optical properties are all wavelength dependent. The beam attenuation coefficient $c(\lambda)$, which is the total light lost from a beam penetrating into a water surface, is the sum of scattering $b(\lambda)$, from suspended matters and molecular water, and absorption $a(\lambda)$ of light, by suspended and dissolved matters and water itself. So, the relation of beam attenuation coefficient and other IOPs is:

$$c(\lambda) = a(\lambda) + b(\lambda) \tag{1.1}$$

AOPs depend on the IOPs and also the angular radiance distribution of the incident light in the water medium. Basic AOP components relative to ORS are irradiance reflectance values and various diffuse attenuation coefficients. The Radiative Transfer Equation makes a connection between the IOPs and the AOPs [20]. Thus, it is the basis for relating remote sensing reflectance (Rrs) to concentrations of OAC of water which cause scattering or absorption of light energy. The basic equation RTE is:

$$R_{rs} = G(\lambda)\frac{b_b(\lambda)}{a(\lambda) + b_b(\lambda)} \tag{1.2}$$

$$a(\lambda) = a_w + a^*_{ph}(\lambda)C_{chl-a} + a_{CDOM}(\lambda) + a^*_{NAP}(\lambda)C_{NAP} \tag{1.3}$$

$$b_b(\lambda) = 0.5b_w(\lambda) + b^*_{b,ph}(\lambda)C_{chl-a} + b^*_{b,NAP}(\lambda)C_{NAP} \tag{1.4}$$

where $G(\lambda)$ is a geometrical scaling factor, $a(\lambda)$ is total water absorption, C_{chl-a} is the concentration of Chl-a, C_{NAP} is the concentration of NAP, a_w and $a_{CDOM}(\lambda)$ are the absorption of water and CDOM, $a^*_{ph}(\lambda)$ and $a^*_{NAP}(\lambda)$ are the specific absorption coefficient of phytoplankton and non-algal particles, respectively. Also, $b_b(\lambda)$ is the total backscattering coefficient, which similarly is composed of scattering terms for water itself, phytoplankton, and NAP [21,22].

The above two equations are based on the influence of the key water components including, NAP, pure water, CDM, and phytoplankton. Initially, most of the bio-optical models for the extracting of water constituents are based on these equations [23]. Given that water is often optically complex water, a function of any of the three main OAC may overlay another. Therefore, water types have more requests for instruments with high spatial and spectral resolution, radiometric sensitivity, high accurate atmospheric correction, and water constituents retrieval algorithms [24].

1.4 Motivation

In Chl-a studies, remote sensing systems offer a wide regional coverage and high temporal resolution, which are essential for long period monitoring. Problems have arisen for the case II waters where Total Suspended Sediments (TSS) and CDOM have higher concentration and their absorptions and scattering do not always have correlation with phytoplankton, and all components existing in these waters will influence the water optical properties. Therefore, the overlying absorptions by DOM and NAP in the blue part affect the blue-to-green based methods, resulting in unsuitability for measuring Chl-a concentration. This prompted, Chl-a retrieval algorithms to emphasise the spectral bands in the red and near-infrared (NIR) spectral regions which have become common for retrieving Chl-a. These Chl-a retrieval algorithms are parameterized to fit sensor channels. Accordingly, they can frequently be used for estimating Chl-a concentration over the case II waters. One of the optical satellites most used for these studies is the Medium Resolution Imaging Spectrometer (MERIS). MERIS had spectral bands situated specifically to measure Chl-a. However, in 2012, this sensor stopped remote transferring data to the Ground. Ocean and Land Color Instrument (OLCI), continuing for MERIS, and Sentinel-2 MSI are current instruments with potential to conduct Chl-a studies. New satellite products have to be tested with ground data. Thus, the main motivation of this research was to examine two current Chl-a retrieval products, Fluorescence Line Height (FLH) and Maximum Chlorophyll Index (MCI) using Sentinel-3 and Sentinel-2.

1.5 Objectives

The European Space Agency has developed free open-source toolboxes for Sentinel-3 and Sentinel-2. Add-in thematic water processing, there are the processors for OLCI and MSI provide the possible routine enhanced interpretation of water-leaving signals over case II waters. Two Chl-a related products, the FLH and MCI, to the sentinel toolbox used to compute the Chl-a fluorescence and scattering peaks by measuring the height of peaks above a specific baseline. The two main objectives of this thesis were to test the suitability of these two products for estimating Chl-a concentration with the new sensors in optically complex water; and to test the value of Sentinel-3 and Sentinel-2 images with in situ measurements and assess the suitability of these sensors to monitor lakes susceptible to intense algal and harmful algae blooms.

1.6 Thesis structure

Following this general introduction which explains the necessity of measuring phytoplankton Chl-a, the logic of using satellite images, and the research motivation and objectives of this thesis, Chapter 2 overviews bio-optical modelling for inland water evaluation and then details on bio-optical modelling of phytoplankton Chl-a. Retrieval algorithms and past and current remote sensing sensors used for monitoring phytoplankton are examined. In situ data for satellite system and algorithm development and validation are also presented. Chapter 3 includes the study area, data set, methodology, results, discussion, conclusion, and recommendations of this thesis.

Chapter 2

Background

2.1 Bio-optical modeling

In 1975, after the launch of the Earth Resources Technology Satellites 1 (ERTS-1), Gorden et al. [25] obtained the first bio-optical model using Monte Carlo simulation of the RTE to build a correlation between AOPs and IOPs. Subsequently, many bio-optical models have been developed for the aquatic system and can be defined in two ways. First, these models can be defined based on the aim of describing the biogeochemical state of the water system. This occurs developing a relationship between radiometric measurements and water constituents to drive information about physical, biological, geochemical processes in the aquatic systems in various ways which mostly using statistical approached [26]. The second way is based on using RTE to drive quantification of IOPs of OAC of water [27], then drive the OAC concentration through analytical approach, for instance, a ratio between their absorption coefficient and specific absorption coefficient or backscattering coefficient to specific backscattering coefficient.

Based on their formulations and their combination with multi-observational platforms such as in situ, airborne, and space bore, bio-optical models can be classified in five groups [28]: empirical, semi-empirical, semi-analytical, quasi-analytical, and analytical. Table 2.1 displays a description of strength and weakness of these approaches.

Table 2.1: Strengths and weaknesses of bio-optical models

	Strengths	Weakness	Ref.
Empirical	- Computational simplicity - Easy to develop	- Not consider physical properties , IOP and AOP - Site and time base for certain parameters - Necessity of in situ data	[29]
Semi-Empirical	- Physical-empirical base - Easy implication	- Inverse solution - Still need Recalibration for different site - Need in situ data - Less physical base	[15]
Semi-Quasi-Analytical	- More physical base - Limited assumptions required - More site transferable	- Need SIOPs - High accurate atmospheric correction - Substantial field work, computing and large training set	[30] [25] [16]
Analytical	- Physical base and more robust - has a unique solution - site transferable	- Knowledge on physical properties of water and boundary condition - Rigorous set of equations - Computer time spend on the numerical calculations - High accurate atmospheric correction	[31]

Empirical and semi-empirical methods are based on the statistical relationships between radiometric data and field measurements. The main difference between these two categories is the assumption made during their development. The empirical approaches try to develop the best correlation between in situ measurements and remote sensing data focusing only on statistical estimation; they do not consider any physical or principal optical properties of water, such as IOPs or AOPs. Empirical methods use statistical techniques such as ANN, stepwise regression and many iteration techniques to provide a best fit between radiometric data and field measurements. On the other hand, semi-empirical methods consider physical properties of constituents such as IOPs and their spectral features, for example absorption coefficient or backscattering coefficients. For instance, a common assumption considered in semi-empirical models for Chl-a estimation is to use the Red-NIR band because of the low combination of water and Chl-a absorption, which causes the scattering to be more noticeable in the reflectance signal. The output of semi-empirical methods still needs recalibration using statistical estimators.

Semi-analytical and quasi-analytical methods, in comparison, are based on the inversion of RTE to make a connection between AOP and IOP following several analytical and empirical procedures. The model inputs AOPs (e.g. water leaving reflectance $R_{rs}(\lambda)$) to compute IOPs. The IOPs estimated from the semi-analytical and quasi-analytical methods are verified with the IOPs of in situ water constituents estimated through analytical methods; for instance, inversion of the ratio of $a_{ph}(\lambda)$ to specific absorption coefficient of phytoplankton $a^*_{ph}(\lambda)$ is used in case of Chl-a estimation [16, 25].

$$Chl - a = \frac{a_{ph}(\lambda)}{a^*_{ph}(\lambda)} \tag{2.1}$$

The main difference between semi- and qausi-analytical methods is the steps applied to compute IOPs. For example, in the case of semi-analytical, $a(\lambda)$ is derived from the sum of absorption of all OAC, $a_{ph}(\lambda)$, $a_{NAP}(\lambda)$, and $a_{CDOM}(\lambda)$. However, in the case of quasi-analytical other OAC absorption is not required, as $a(\lambda)$ first derives from R_{rs} directly and then the other OAC absorption coefficients are calculated from the decomposition of computed $a(\lambda)$ [32].

Table 2.2: Formulation of different types of bio-optical models

Method	Equation	Ref.
Empirical	$log(SD) = a(TM1/TM3) + b.TM1 + c$	[34]
Semi-Empirical	$[R_{rs}(665)^{-1} - R_{rs}(708)^{-1}]R_{rs}(753)$	[35]
Semi-Analytical	$a_{pc}(620) = \left[\left(\left[\frac{R(709)}{R(620)}\right][a_w(709) + b_b]\right) - b_b - a_w(620)\right]\delta^{-1}$ $- [\epsilon a_{chl}(665)]$	[36]
Quasi-Analytical	$a_{tw}(\lambda) = \dfrac{R_{rs}(709)b_b(\lambda)[a_w(709) + b_b(709)]}{R_{rs}(\lambda)b_b(709)} - b_b(\lambda) - a_w(\lambda)$	[32]
Analytical	Inversion of a R_{rs} model	[31]

Analytical models are a forward or direct problem of RTE and based on physical characteristics of biological materials that first analyze, and then predict the optical properties of constituents. These type of bio-optical models are based on the fundamental theories of optics which apply to a single matter using several equations [33]. For instance, at the level of a single phytoplankton cell, the extension of IOPs of a cell to a population of cells is a direct problem from a conceptual and numerical perspective. It can start with using fundamental information about physical properties of the cell (pigmentation, cell size, intercellular and chemical structure, specific absorption of substances, index of refraction) to drive the IOPs that parametrize the fundamental information. Then, the computed bulk of IOPs and the physical properties of the boundaries (such as the illumination conditions at the surface, properties of bottom reflectance) are used to solve RTE through a complicated math equation to find the radiance distribution. Finally, radiance distribution can be computed for the bulk of AOPs of interest.

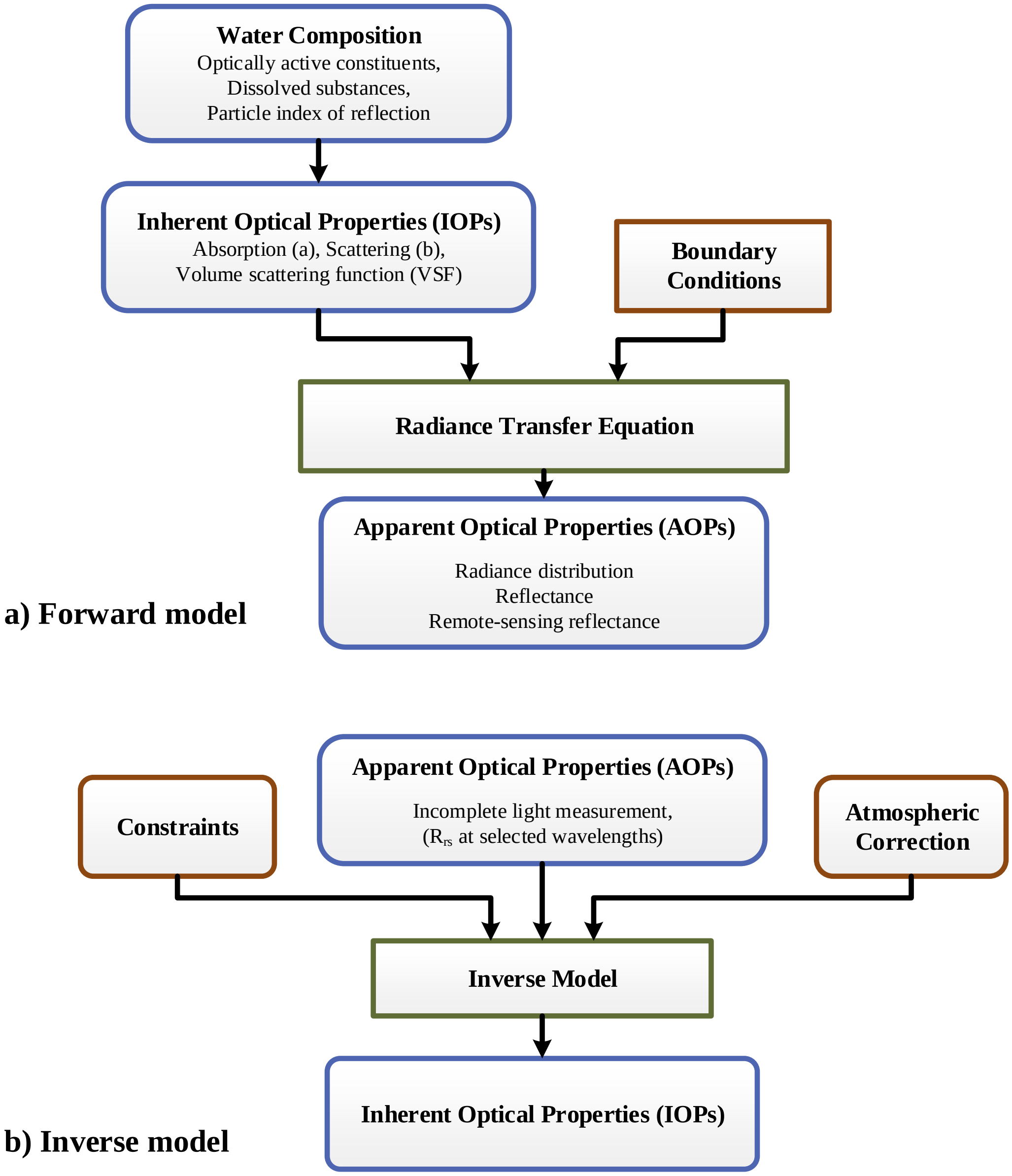

Figure 2.1: The conceptual process involved in solving: a)the forward radiative transfer problem, b)the remote-sensing inverse radiative transfer problem [7].

2.2 Bio-optical modeling of phytoplankton Chl-a

The light interacting with algae or cyanobacteria can be changed through scattering, fluorescence, and absorption. Bio-optical modeling describes these interactions and obtains information about optical properties of the phytoplankton and biological characteristics (such as size, cellular structure, pigmentation) which govern these changes. Given that phytoplankton is a microscopic, single cellular organism drifting on the surface water, it cannot be observed by human eyes or sensors. And in fact, a bulk effect of more than hundreds of cells are what human or remote sensors observe. Therefore, the interaction of bulk cells with light might be described by the theory of single particle scattering, which is a framework to understand the microscopic level of light interaction with a single cell and present the fundamental theories needed for Chl-a bio-optical modelling.

Phytoplankton cells are considerably variable in size, from less than 1 μm to larger than 10mm. The cells are not only vary by 6 orders of magnitude in size but can be seen in the form of unicells to a cluster of cells, filaments or colonies. The structure of cells can be different between each phytoplankton species and show different behaviors. For instance, in diatoms silica cell morphology or in cyanobacteria gas vacuoles. Despite diversity in size, form, structure, and behavior that influence the specific optical properties of the phytoplankton, all phytoplankton species contain a green pigment Chl-a. Chl-a is an essential indicator for estimating phytoplankton biomass and lake productivity using Chl-a bio-optical models. These models estimate Chl-a through three pathways: phytoplankton absorption, fluorescence, backscattering.

2.2.1 Absorption

The spectral absorption coefficient of phytoplankton $a_{ph}(\lambda)$ is a combination of Chl-a and other accessory pigments which vary in shape and magnitude. The maximum absorption of Chl-a is seen in blue (440 nm) and red (675 nm) spectral wavelengths. $a_{ph}(\lambda)$ is related to Chl-a absorption in these two spectral regions in the broad range of 0.01 to 10000 $mg\, m^{-3}$ [37]. Phytoplankton absorption and its dependence on the Chl-a concentration, symbolized as Chl-a specific (i.e., per unit of Chl-a concentration) absorption coefficient, ($a^*_{ph}(\lambda)$), is essential for bio-optical remote sensing models to retrieve Chl-a concentration. However, phytoplankton absorption normalized to Chl-a ($a^*_{ph}(\lambda)$) displays variability controlled by a pigment packaging effect and to a less degree, cellular pigment composition [37]. Pigment packaging is predicted by theory [38] and depends on cell size and the concentration of intercellular pigments. Variation in pigment composition and packaging result from population changes or amount of light received by the population, nutrient concentration, and other environmental factors. Therefore, in some cases, an inverse relation between Chl-a and $a^*_{ph}(\lambda)$ is observed when the larger cells dominate the phytoplankton population at high levels of Chl-a concentrations [38]. In addition, this relationship may also be affected by high community of small-cell cyanobacteria due to their different intercellular structure as a prokaryotic cell.

A further reason that measuring phytoplankton absorption by passive sensors is challenging relates to the low signal to noise ratio of Chl-a absorption bands (440, 670 nm) [39]. In vitro, the pigment is first extracted from the sample through organic solvents; then the absorption and backscattering of a controlled light beam measured by a lab spectrophotometer. However, in remote sensing, measuring the wavelength incident with the pigment has a very small signal to receive to the sensor, particularly in a high Chl-a concentration. Consequently, the low signal causes a high error for measuring absorption especially in blue bands. The blue band is limited to measuring the absorption of Chl-a in low concentration, less than 1.5 $mg\, m^{-3}$ [40]. Although the reflectance of 665nm is insensitive to increasing Chl-a concentration, many algorithms have been developed based on Chl-a absorption focusing on the blue bands.

One of the simplest algorithms is the empirical algorithm related to the ratio of blue/green bands (normalized to increase the SNR). This ratio is based on the assumption of the increasing absorption in the blue bands (near 440 nm) with the increase in the Chl-a concentration (take into account the theoretical threshold of unpackaged Chl-a absorption is 0.027 $m^2 mg^{-1}$ [41]). For instance, many blue/green ratio algorithms (e.g., SeaWiFS, MODIS, MERIS, OLCI products) have shown an effective result for the ocean and some clear lake waters. The MERIS (OC4Me) product [42], which is not purely empirical, remains the most effective empirical approach and has been used globally for ocean color.

In case ll waters that have absorption of other constituents, the blue reflectance is affected by other components such as CDOM, suspended organic and inorganic particulates. For instance, humic acid, as a principal component of humic substances used as a soil supplement mostly in agriculture, strongly affects the $a_{ph}(\lambda)$ at around 440 nm. The absorption of tripton, suspended inorganic matter, is the same as CDOM in the blue band [43]. Because of this extra absorption, simple empirical correlation of the ratio and Chl-a is unsuccessful. Several IOP inversions (inversion of bio-optical physical models) attempt to retrieve the other absorption coefficient of water constituents from Rrs [44], or through alternative nonlinear optimization approaches, such as ANN to indirectly estimate Chl-a [45]. However, the retrieval of Chl-a from the IOP inversion (based on the above discussion) has uncertainty when Chl-a concentration is derived from a_{ph} through the ratio of a_{ph} to a^*_{ph}. The nonlinear optimization approaches that estimate Chl-a through local parametrization might have the advantage of using the entire spectrum, but do not consider IOPs or physical knowledge of the water system. These methods while using synthetic training of datasets, try to estimate Chl-a through statistical and mathematical procedures [8].

From the sensor design perspective, absorption-based methods required a very high SNR in the selected bands and also precise channels for the atmospheric correction. Aerosol absorption and scattering highly influence the blue region of the spectrum. These will be more complicated when the NIR spectra cannot be assumed dark pixel due to particulate backscattering radiances for atmospheric correction approaches. Although these requirements are configured in the ocean sensors, such as MODIS, MERIS, OLCI, etc., the spatial resolution of these instruments limits their performance since the full resolution band has not the same SNR of the reduced resolution. Atmospheric correction algorithms have improved the Chl-a retrieval methods consequently using the absorption approach (Chl-a less than $0.1\, mg\, m^{-3}$) and combined absorption with the other pathway approaches (Chl-a less than $10\, mg\, m^{-3}$) for the ocean and clear waters [46].

2.2.2 Fluorescence

When a phytoplankton pigment absorbs a photon of incident light, the molecule is elevated from its ground state to its singlet excited state. The excited molecule returns to the ground state in three possible ways. It can be passed to photochemical reaction centers (photosystems 1 (PSI) and 2 (PSII)) and use in the photosynthesis processes. And, the balance of the energy is emitted as a photon (fluorescence), named photochemical quenching, or in the presence of excess light is emitted as heat (non-photochemical quenching). Both NPQ and fluorescence are photoprotective mechanisms which reduce the excess energy [47].

In algae a series of pigment-protein complexes from light-harvesting complexes (LHC) embedded on the thylakoid membrane transfer the absorbed light to the PSII and PSI to be used in photoprotective mechanisms. In the low light states, they absorb light and move the excitation energy to the photosystem reaction center; in the high light condition, by dissipating the energy as heat they perform a role as a photoprotection reaction to decrease the excited state lifetime of the pigments.

The variety in chloroplast pigmentation of phytoplankton is very large. The pigments of photosynthetic microalgae comprise 10 different Chlorophyll (such as Chl-c, Chl-a, Chl-b, and divinyl a and b), less than 30 major carotenoids (such as carotenes and xanthophylls), and three main groups of phycobilins (such as allophycocyanins, phycocyanins, and phycoerythrins [48]. In a microalgae chloroplast organelle, these pigments are bonded to proteins forming various pigment-protein complexes that have variable taxonomy. These diverse pigment-protein complexes cause different photobiological responses (processes that involve the interaction with light). They subsequently impact the photophysiological characteristics of the species, for example, light harvesting, photoprotection, photoacclimatisation, and photoadaptation [49]. In fact, the variability in pigment-protein of LHCs is responsible for the variability of the absorption coefficient and fluorescence spectral shape in a different type of phytoplankton species [50].

Phytoplankton also displays substantial intraspecific variation. For instance, the same species might have different pigment content that is mostly due to photoacclimation, adjustments in the photosynthetic pigment content in response to a light condition to maximize growth rate in a different light environment (e.g., irradiance, spectral composition, and day length) [51]. Or, more light-harvesting pigments will be seen in cells which grow in a low light condition than high light. The studies have shown that intraspecific variation is also seen due to photoacclimation plasticity (adapted to high irradiance) which affects bio-optical spectral characteristics among species. The difference between these two photo-physiological characteristics is that photoacclimation does not change the genetic structure of the species, however photoacclimation plasticity does [52].

A case study is the large raphidophyte Gonyostomum semen, a nuisance freshwater microalgae which has expanded to several new habitats and currently dominates the algae population in many lakes worldwide. The bloom causes allergic reactions due to mucus threads and trichocysts in people swimming in the lakes and also clogs filters for water treatment [53]. Past evidence showed that this expansion and high competitiveness of G. semen with other algae happened for several reasons: first, environmental variables, mainly temperature and the length of the growing season, watercolor (e.g., ongoing brownification of waters), and lake morphometry [54]. Second, manipulation of food cycles (e.g., biomanipulation of algal blooms through selective removal of zooplanktivorous fish [55,56]). Third, multiple variables that make a favorable condition for the phytoplankton (e.g., increased concentrations of DOC, low PH, high Phosphors [57]), and also its distinct ability to migrate through water column [58]. The new studies [59], however, are showing that changes in the photophysiology of G. semen (e.g., Pigment composition, photoadaptation to turbid waters, photoacclimation reactions to light climate) are the keys to its ecological success compared to other phytoplankton species and strains of Raphidophyceae. This raphidophyte species was previously able to photosynthesize in a very low light condition because of having enhanced light harvesting system, however, with lack of enough photoprotective capabilities since they were able to migrate in water layers in high intensity. Then, through time living in diverse habitats and light conditions, G. semen saw significant alterations in pigment ratios within the strains due to genetic adaptation to the different situations. For instance, in addition to the pigments already known for the raphidophytes species, studies identified a new pigment, named Alloxanthin, that has not seen in raphidophyte species before. This finally indicates an enhancement in photoprotective functions in the species. As result, the regulation of pigment content and the variability in Pigment composition have changed the bio-optical signature of G.Semen strain [50].

With regard to pigment composition, PSII and PSI are stable and insensitive to photoacclimation; therefore, as previously discussed, most of the variability is due to pigment-protein complexes from LHCs (which transfer absorbed light to the reaction center complexes in PSII and PSI). In an algae cell, PSII and PSI are two of the components of photosynthesis. Both contain LHCs and the bulk of the pigments that located in. Chl-a, as well as the Chl-a, bind to different protein complexes, and have different absorption and fluorescence features. In vivo, it is shown that Chl-a fluorescence emission in the red region is a function of excited wavelengths associated with the different wavelengths of light absorbed by PSII. Chl-a fluorescence in PSll is near 685 nm and at the longer bands (730-740 nm),whereas in PSl, all light is emitted at wavelength longer than 700 nm.

In eukaryotic phytoplankton, PSll contains more than 80% of the Chl-a pigments. Thus, the LHCs pass a high amount of absorbed light to this section, subsequently constituting 95% of the PSll fluorescence emission . Since Johnsen et al. [60] found that fluorescence excitation at the red region emission is related to the fluorescence of Chl-a in the PSll only, studies have focused more on Chl-a fluorescence measurement around 685 nm. However, in prokaryote phytoplankton, cyanobacteria, Chl-a pigments (up to 70%) are contained in PSl which fluoresces light at wavelengths longer than 700 nm. This difference mainly related to different levels of pigment composition among phytoplankton groups which is highest between prokaryotes and algae [61]. In cyanobacteria, phycobilipigments are the primary light-harvesting complexes that pass the excitation light to either PSI or PSII, and they consist of pigments such as phycoerythrin, phycoerythrocyanin, phycocyanin, and allophycocyanins. State transition (physiological mechanism that regulates absorbed light between PSll and PSl) in the cyanobacteria photosystem flows the excitation light to the PSl; consequently, fluorescence emission reduces from PSll. Thus, in cyanobacteria the intensity of fluorescence signals is very low, around 685 nm compared to in algae [61].

Photochemical quenching is an active process, and fluorescence signals emitted from phytoplankton cells are observed by the sensor. Chl-a estimation using fluorescence approaches is based on the assumption that Chl-a concentration is proportional to received signals. This assumption is valid for algae cells since 80% of the Chl-a is in the PSll. However, it is not accurate in the case of cyanobacteria [62] (as discussed above). Wynne et al. [63] noted that in water dominated-cyanobacteria, a significant trough is seen near 685 nm. Therefore, going forward our discussion will be limited to the algal fluorescence, with respect to other methods required for cyanobacteria detection (e.g., considering PSl emission [61]).

In vivo, Chl-a fluorescence is measured by devices that detect the effective quantum yield from PSll near the 680 nm wavelength under a precise illuminated beam. Factors such as light intensity, intercellular absorption, and fluorescence emitted from the PSll, are assumed to be constant [64] [45]. Thus, the method gives a rough estimation of Chl-a . However, in vitro, Chl-a measurements are more precise and the assumptions are mostly accurate because Chl-a is dissolved in an organic solvent at a given temperature. In the real environment (nature) when the phytoplankton absorbs sunlight energy, Chl-a fluorescence (named sun-induced fluorescence, SICF) is highly variable and depends on the physiological status of the cells, the presence of other phytoplankton species, and the spectral distribution of irradiances.

Fluorescence Line Height Algorithm (FLH)

Given that the Chl-a is proportional to the SICF emission, many studies started to examine its validity to measure Chl-a concentration in coastal waters. Results showed a good correlation between Chl-a and SICF (e.g., [65–67]). These researches led to the configuration of a few bands on the ocean satellite sensors (such as MODIS, MERIS, GOCI, and OLCI). These bands are positioned slightly differently in each sensor, but they are all located in the red-edge region, one close to the fluorescence peak and two bands outside of the fluorescence peak which aim to extract fluorescence radiance through a fluorescence light height (FLH) algorithm [68]. The FLH algorithm estimates the extra reflectance in the fluorescence peak band above a baseline. This baseline connects two reflectance bands positioned outside of the fluorescence peak. This algorithm is identified as [69].

$$FLH = L_2 - [L_3 + \frac{(L_1 - L_3)(\lambda_3 - \lambda_2)}{\lambda_3 - \lambda_1}] \tag{2.2}$$

where L_1, L_2, and L_3 are radiances at wavelengths λ_1, λ_2 and λ_2, respectively.

The FLH algorithm is more accurate when used for case I and oligotrophic waters. This is because the atmospheric correction works better for ocean waters, and also the elastic scattering signals are low above the baseline curve. Recently, in inland waters, with the improvement of atmospheric algorithms, turbidity is the main source of reducing the sensitivity of the FLH algorithm. The reflectance peak around 700 nm influences the fluorescence peak around the 685 nm retrieval. This reflectance peak is related to increased water absorption, decreased Chl-a absorption, increased particulate backscattering in this spectrum region [70]. Despite CDOM absorptions ($\sim$440 nm, $< 1\ m^{-1}$) having low effect on FLH signals, suspended sediments ($5\ gm^{-3}$) result in significant error due to the particulate scattering. Moreover, FLH application in high phytoplankton biomass ($> 20\, mgm^{-3}$ [68]) is hindered by a peak reflectance overlapping the fluorescence reflectance. This peak shifts to the longer wavelengths with increasing Chl-a concentration (e.g., to 705 nm at 100 $mg\,m^{-3}$). Therefore, the FLH algorithm is more applicable for oligo to mesotrophic waters less than 20 $mg\,m^{-3}$ [71].

Accurate result from the FLH algorithm will require high radiometric sensitivity (SNR), a precisely located narrow bandwidth, and bands related to atmospheric correction.These criteria to some extent are configured to the ocean sensors such as MODIS, MERIS, OLCI [72]. In addition, fluorescence light detection and ranging (LiDAR) has shown a potential for Chl-a measurements in case ll [73]. Despite the sensitivity of FLH to the atmospheric effects, the FLH algorithm effectively normalizes atmospheric signal effects, in addition to selecting FLH bands having proxy of less than 100 nm [62]. Therefore, FLH methods prove not to rely on aerosol correction (atmospheric corrections take account Rayleigh scattering and absorption) in waters with small NIR reflectance [74].

2.2.3 Scattering

Phytoplankton or particulate backscattering ($b_{b,ph}$) is the third approach to indirectly estimating Chl-a concentration, in addition to the two direct approaches of absorption and fluorescence. Measurement of optical backscattering of phytoplankton may require of use

Mie scattering theory as phytoplankton cells assume a spherical homogeneous sphere [75]. However, this assumption has been repeatedly criticized [76] due to its simplicity and inadequate reproducing the backscattering of phytoplankton cells [77]. Light scattering by phytoplankton requires more sophisticated models (e.g; two or three layer models) which consider the complex cellular structure of phytoplankton such as external (e.g. cell wall) and internal (e.g. chloroplast)cell structures [78].

The spectral variability of scattering properties is very large between and within the phytoplankton species. This is basically due to the difference of particle cell shape and size (particle cell distribution), morphology, and internal structure (real refractive index) in different phytoplankton cells. Laboratory measurements of scattering properties of phytoplankton species appear strongly peaked in forward direction and weakly (less than 1 %) scattering in backward directions. Since observed reflectance is proportional to forward scattering, backscattering of phytoplankton is the interest to be used in the Chl-a measurements [79].

Studies have shown that the morphological and structural features of the phytoplankton cell have the most significant role on their light-scattering properties [5]. For instance, algae have more complex internal structures (e.g chloroplast, chromosome, bacillariophyceae) compared to cyanobacteria that have less internal structure. In contrast, the honeycomb-like structure gas vacuoles of cyanobacteria remarkably influence the behaviour of scattering and increase its magnitude and spectral features [80]. In addition, the gas filled vacuoles help cyanobacteria to float very near the water surface, which causes to increasing brightness and reflectance signals [62]. This specific structure of cyanobacteria can be used as the main indicator for distinguishing from algae [81]. There are also species surrounded by silicate mantels such as silica cell walls in diatoms which strongly influence the backscattering coefficient.

On the other hand, studies show that scattering does not depend on the cell size, and in some case studies show an inverse relationship between backscattering coefficient and cell size [82]. nevertheless, some evidence has shown a positive relationship of cell size and backscattering in dinoflagellate; however, some researchers have argued that low reflectance in dinoflagellate bloom might be due to the algaes ability to regulate in the water column, and high backscattering values might be from other species present such as cyanobacteria or detached structures [83].

Normalizing backscattering of phytoplankton to the Chla-specific backscattering coefficient ($b^*_{b,ph}(\lambda)$) use to determine the mass concentration of Chl-a (derived from phytoplankton cells). For instance, $b_b(\lambda) = c\, b^*_{b,ph}(\lambda)$ (unit $m^2\, mg^{-1}$) which range from 0.02 related to the low scattering algae cells to $12 \times 10^{-3} m^2\, mg^{-1}$ related to the dinoflagellates and cyanobacteria (Trichodesmium) due to their specific cellular structure (as previously discussed) [25].

Observations of phytoplankton cultures show that different phytoplankton groups and community structure have different particulate size distribution, cellular morphology and composition which together lead to a highly species-specific relationship between Chl-a and $b_{b,ph}$ relationships [83]. In fact, these relationships are based on the particulate characteristics of cells without any interaction directly with the cell pigments. Furthermore, coenobium (colony of algal cells) also influence the Chl-a and $b_{b,ph}$ relationships. In another words, with increase in density of the cells backscattering of the cellular material increases as well as the Chl-a concentration.

Quibell [84] indicates that remote sensing of algae in case II waters is based on increased scattering by the phytoplankton cells, not increased absorption by Chl-a. Subsequently, many studies have examined approaches based on algal backscattering [85]. The results admit that this bio-optical relationship, $b_{b,ph}$ vs. Chl-a relationship, is significant and best described, particularly in distinct regimes and types. Phytoplankton backscattering signals can be noticeable in inland waters with Chl-a larger than 10 $mg\, m^{-3}$, which contribute distinct peaks around 560 and 700 nm [70, 71]. However, the scattering from red-edge is preferred over the peak near 560 nm. This is due to the CDOM and other accessory pigments influences on the shorter wavelengths.

Chl-a concentration has a strong correlation with the height and position of the red reflectance peak. This peak shifts to longer wavelengths as Chl-a concentration increases. The peak reflectance in the red-edge results from increased water absorption in the longer bands ($>$ 700 nm), the influence of Chl-a absorption and fluorescence bands at 665 nm and

680-690 nm, respectively [68]. In addition, recent studies show that absorption and fluorescence also contribute to the the shift of the peak position to the longer wavelengths [68], and also the results displays a specific relationship associated by species types. For instance, cyanobacteria has a depression in the reflectance at 680 nm [62, 63].

The ratio of reflectance around 700 nm to 670 nm, drives the simplest red-edge scattering-based algorithms used effectively to determine Chl-a in high biomass waters. Furthermore, a strong correlation ($R^2 > 80$)is shown between the ratio and Chl-a [68]. More pronounced ratio forms are the three-band algorithm proposed by Gitelson et al. [35] or four-band algorithm by Le et al. [86], with an added band near 700 nm. The additional band is included to improve the three-band algorithms and reduce the effect of scattering of suspended matter in the NIR region. The Normalized Difference Chlorophyll Index (NDCI) has proveded better results compared to two- and three-band NIR models for most of the sensors such as MERIS, MODIS, WorldView-2, and OLCI Sentinel-3 [87]. Modified FLH algorithms are the peak height models, such as the reflectance line height (RLH) [88] or scattered line height algorithms [71] which are better suited to highly turbid waters showing $R^2 > 0.85$ [89].

The most current used red-peak scattering-based algorithms for waters with high Chl-a concentrations are the MCI, which use the RLH model and the 709 nm band [90], the Maximum Peak Height (MPH) [62], which is developed to determine trophic status and indication of potentially harmful phytoplankton blooms (peak between 680 and 750 nm bands), and the Adaptive Reflectance Peak Height model (ARPH) for HICO [91] which is derived using bands centered at 690, 696, 702 and 708 nm. These algorithms can also drive using RTE, utilizing Chl-a specific absorption and backscattering coefficients [68, 92].

An algorithm developed for MERIS, the Cyanobacteria Index (CI), proposed by Wynne et al. [95] is based on the replaced fluorescence peak with a distinct trough at 681 nm. The CI is an FLH algorithm that is used which measures the depth of the absorption trough at 681 nm using 709 and 665 nm bands to connect the baseline curve. The positive values of the CI are considered an indication of presence cyanobacteria. However, this assumption may not be valid, since the lack of signal might be related to high scattering and absorption

Table 2.3: Some of the most current scattering based Chl-a retrieval models.

Equation	λ_1	λ_2	λ_3	Ref.
$Chl-a \propto \frac{R_{rs}(\lambda_2)}{R_{rs}(\lambda_1)}$	665	708		[93]
$Chl-a = [R(\lambda_1)^{-1} - R(\lambda_2)^{-1}]R(\lambda_3)$	670	710	750	[35]
$Chl-a \propto \frac{R_{rs}(708) - R_{rs}(665)}{R_{rs}(708) + R_{rs}(665)}$	665	708		[87]
$MPH^{*} = R_{max} - [R_1 + \frac{(R_3 - R_1)(\lambda_{max} - \lambda_1)}{\lambda_3 - \lambda_1}]$	665		885	[62]
$RLH^{**} = L_2 - L_1 - \frac{(L_3 - L_1)(\lambda_2 - \lambda_1)}{\lambda_3 - \lambda_1}$	670	700	850	[88]
$MCI = L_2 - k^{***}[L_1 + \frac{(L_3 - L_1)(\lambda_2 - \lambda_1)}{\lambda_3 - \lambda_1}]$	680	708	753	[94]

$^{*}R_{max} = max(R_{681},\ R_{709},\ R_{753})$
** L_i is radiance in band i=1,2,3, *** $k = 1.005$

effects.

Like the FLH model, the red-edge peak scattering-based algorithms have the advantage of insensitivity to atmospheric effects, spectral proximity, and ability to detect high reflectance signals from high-biomass waters. Different correlation methods (such as linear, polynomial, power law, quadratic, etc.) are applied to make a relationship between Chl-a and these models.

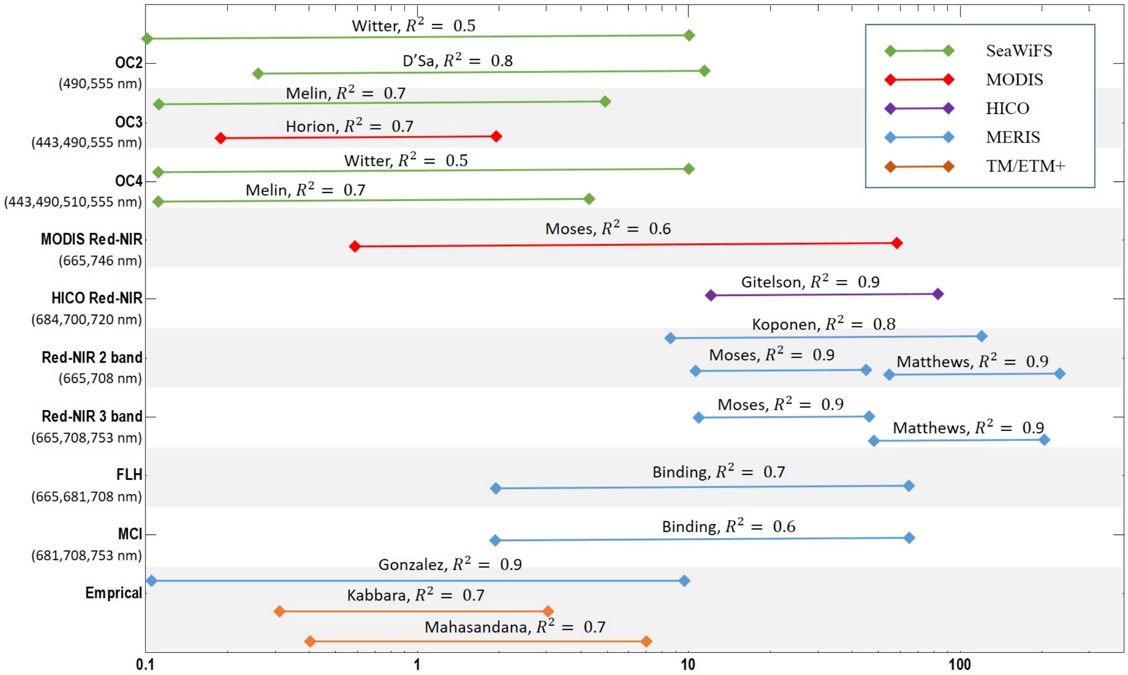

Figure 2.2: Comprehensive overview of all recent band arithmetic Chl-a retrieval applications (source: figure 1.1 Odermatt et al. [8]).

2.2.4 Chl-a retrieval algorithms

Odermatt et al. [8] provided a comprehensive overview of all recent band arithmetic Chl-a retrieval applications using optical satellites such as SeaWiFS, MODIS, MERIS, Landsat, and HICO to compare various methods and corresponding sensors for Chl-a retrival methods. Figure 2.2 presents a summary of 2006-2011 published papers using the semi-empirical and empirical methods for Chl-a estimation in different concentration ranges. Additionally, Blondeau-Patissier [96] discuss and compare different algorithms types used for the detection, mapping, and analysis of phytoplankton blooms from various sensors. Table 2.4 displays some different forms of spectral bands used by algorithms from the blue-green and red-NIR spectral region using ocean sensors such as The Coastal Zone Color Scanner (CZCS), MODIS, MERIS, and SeaWiFS.

Table 2.4: Different band compositions used for CZCS, MODIS, MERIS, and SeaWiFS.

	Product	Sensor	Bands(nm)	Ref.
Band ratio	OC3C	CZCS	443,520,550	[19]
	OC3M	MODIS	443,448, 547	[97]
	OC4	SeaWiFS	443,490,510,555	[98]
Derivative	FLH	MODIS-Terra	667,678,746	[99]
	FLH	MERIS	665, 681, 708.75	[100]
	MCI	MERIS	681, 708.75, 753	[100]
	FAI	MODIS	667, 859, 1240 or1640	[101]
Spectral band difference	CIA	MODIS-Aqua	443, 555 , 670	[102]
	CIA	SeaWiFS	443,555,670	[103]
	NDCI	MERIS	708,665	[87]

2.3 Past and current satellite instruments used for monitoring phytoplankton Chl-a

Most of the satellite sensors used in water remote sensing operate on sun-synchronous low orbit satellite platforms. These satellites acquire data with a spatial resolution of a few meters to more than 1 km and temporal resolution of 1 to 15 days. In the 1970s, passive satellites were first launched to display land and surface water. For example, the Thematic Mapper (TM) (advanced, multispectral scanning, Earth resources sensor) used to retrieve maps of Chl-a [104], and the results showed that in ideal conditions the TM could be used with limited accuracy. The long-term archive Landsat series over 40 years have been helping to study long-term trends in inland waters. For instance, Landsat ETM^+ was used over 10,000 Minnesota lakes to drive a map of Chl-a and other water constitutes [105, 106]. Later improvement of spectral and radiometric sensitivity of sensors, such as NASA Advanced Land Imager (ALI) and hyperspectral Hyperion sensor, improved the retrieval of Chl-a [107,108]. Launched in 1978, the CZCS was the first sensor with a spatial, spectral and radiometric resolution suited for observations over the ocean waters. Many studies used CZCS for dynamic phytoplankton blooms in marine waters, but the unsuitable spatial resolution of the sensor, 825 meters, limited its applicability to large-scale optically complex waters, particularly those with high phytoplankton biomass, such as Lake Michigan [109].

Ocean color sensors followed the CZCS with Sea-Viewing Wide Field-of-view Sensor (SeaWiFS). The SeaWiFS ocean color products for monitoring Chl-a concentration assessed Lake Erie [110]. In 1986, SPOT-1 (Satellite Pour l'Observation de la Terre), enhanced with a relatively high spatial resolution, 10-20 m, followed to SPOT-4 to provide HRVIR (High-Resolution Visible and Infrared) in an improved version with the same 26-day temporal resolution launched by France. In 1999, IKONOS with a spatial coverage of 1 m and temporal resolution of 1-3 days was initiated by a private sector. NASA launched MODIS with a improved spatial resolution of 250-300 m for ocean studies, and have used in numerous large-lake studies of Chl-a; that proved the potential of ocean sensors for large-scaled inland waters, despite their relatively coarse spatial coverage, and improved real-time monitoring applications [111].

MERIS provides an enhanced spatial resolution and additional key bands which have improved remote sensing of phytoplankton bloom monitoring systems [62, 112]. MERIS is a push broom system designed to deliver data while the sky is clear or moderately cloudy. This sensor's characteristics are a field of view of 68.5 around nadir with an 1150 km swath width, 300 m spatial resolution, spectral resolution of 15 bands across the range of 390 nm to 1040 nm (VIS-NIR), and bandwidth between 2.5 and 30 nm [4]. Table 2.5 displays the satellite sensors recently used in phytoplankton studies.

Table 2.5: List of satellite instruments used for phytoplankton Chl-a with their specific characteristics [1].

Satellite sensor	Period of operation	Spatial (m)	No. bands	Radio-metric	Temporal (days)	Swath (km)	Limitation
Landsat 5	1984-2012	30/120	7	8 bits	16	180	
Landsat 7	1999-present	30/60	7	8 bits	16	180	Spect., Temp.
Landsat 8	2013-present	30/100	10	12 bits	16	180	Spect., Temp.
Spot-5	2002-present	10/20	4	8 bits	2-3	60	Spectral, cost
Spot-6	2012-present	6	4	12 bits	2	60	Spectral, cost
Spot-7	2014-present	6	4	12 bits	2	60	Spectral, cost
RapidEye	2008-present	5	5	12 bits	1	77	Spectral, cost
IKONOS	1999-present	3.2	4	11 bits	3.5	11.3	Spectral, cost
QuickBird	2001-present	2.44	4	11 bits	3	16.5	Spectral, cost
GeoEye-1	2008-present	1.65	4	11 bits	4-5	15.2	Spectral, cost
WorldView-2	2009-present	1.85	8	11 bits	1.1	16.4	Cost, swath
WorldView-3	2014-present	1.24/3.7	28	11 bits	4.5	6	Cost
CZCS	1978-1986	825	6	8 bits	Varies	1,566	Spatial, Spect.
SeaWiFS	1997-2010	1,100	8	10 bits	1	2,801	Spatial, Spect.
MODIS–Terra	1999-present	250–1000	36	12 bits	1	2,330	Spatial, Spect.
MODIS–Aqua	2002-present	250–1000	36	12 bits	1	2,330	Spatial, Spect.
HICO	2009-present	90	87	12 bits	Varies	42*192	Experimental
Hyperion	2000-present	30	220	12 bits	Varies	7.5*100	Experimental
MERIS	2002-2012	300	15	12 bits	3	1,200	Spatial
Sentinel-2	2015-present	12–60	13	12 bits	5	290	Spectral
Sentinel-3	2016-present	300	21	12 bits	2.8	1,269	Spatial

2.3.1 Sentinel-3

Sentinel-3 satellite is a European earth observation mission consisting of two satellites: Sentinel-3A launched on 16 February 2016 and Sentinel-3B on 25 April 2018. It is primarily for sea surface topography, temperature, and color application with high accuracy when used in ocean forecasting systems, and environmental and climate monitoring. The mission is continuing the ERS, Envisat and SPOT satellites. Sentinel-3 is a multi-instrument carrying four payloads: Ocean and Land Color Instrument (OLCI), Sea and Land Surface Temperature Radiometer (SLSTR), SAR Altimeter (SRAL), and Microwave Radiometer

(MWR) which is designed for seven-years operational time. The OLCI data include Near-Real-Time (NRT), delivered less than 3 hours after data acquisition, and Non-Time Critical (NTC). The NRT data use the ECMWF meteo forecast data; and NTC products use the ECMWF analysis data, therefore, at Level 1, the difference between the OLCI NRT and NTC data is in the ancillary meteo data.

The OLCI main characteristics are 1270 km swath-width, push broom spectrometer (with five cameras that reduce sun-glint contamination tilting cameras in the westerly direction), 300m spatial resolution, and 21 bands (0.4-1.02 μm) (Table 2.5). The two in-orbit Sentinal-3 satellites have a revisit of less than two days over daylight (sun-synchronous) in full resolution (FR). Figure 2.3 displays three different OLCI products associated with the three processing level: level-0 product generated from level-0 processing which includes unpacking (extract raw data in instrument source packet (ISP)) for quality check, and appending annotation. In this level, the raw input data are checked for synchronization frame, duplicate numbering or invalid packets, etc. and then sorted in time. Next, several quality flags are generated and associated with metadata. These quality flags provide info regarding the nominal, contingency, and degraded processing, and satellite maneuver.

The level-1 product generated from level-1 processing includes TOA radiance which is calibrated radiometrically and characterized spectrally. these are georeferenced, quality-controlled, primarily pixel classified (land, water, cloud masks), and annotated with satellite position through three types of processor (earth observation mode, radiometric mode,and spectral calibration mode). The data are produced in FR (300 m) and Reduced Resolution RR (1.2 km) for the whole earth.

Level-2 products generated from level-2 processing aim to drive geophysical quantities for ocean, land and atmosphere application. The first process is involved with the common pre-processing, including conversion of data from TOA radiances to reflectance, cloud masking, corrections for gaseous absorption (i.e., H2O, O3)and smile effect (variation of the detected wavelength across the field of view), Pixel classification (glint reflectance, land and water), and retrieval of the total column water vapor. Then, based on the nature of the corrected pixel, the products are involved with two primary processes, ocean and land processing. Finally, the output provides expected geophysical products corresponding to

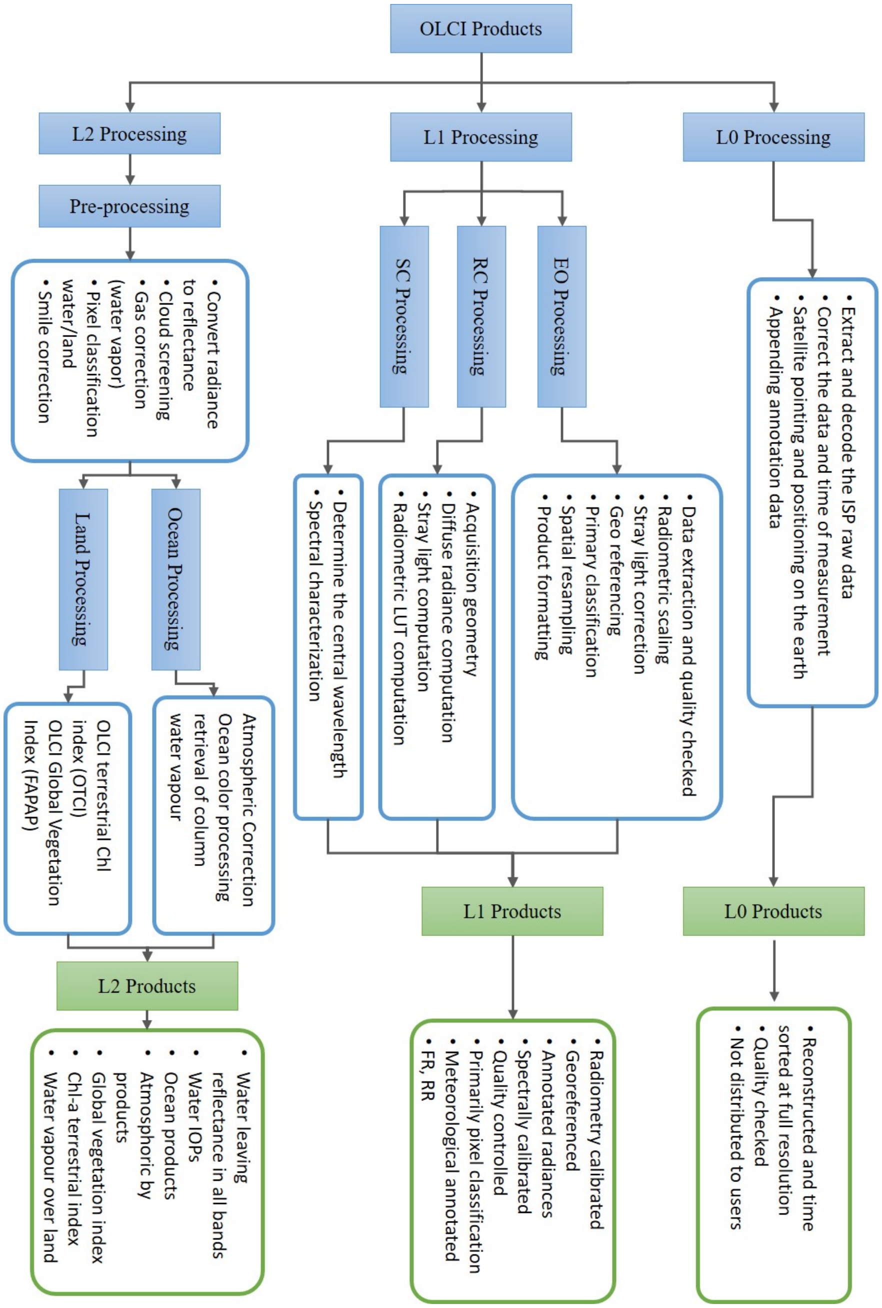

Figure 2.3: A schematic overview of OLCI data processing levels

Table 2.6: List of Sentinel-2 MCI product types available for users.

Product Level	Description
Level-1B	- Radiometrically and geometrically corrected - TOA radiance in sensor
Level-1C	- TOA reflectance - Resampled with a constant Ground Sampling Distance (10, 20 and 60 m) - Include: Land/Water, Cloud Masks and ECMWF (total column of ozone, total column of water vapour and mean sea level pressure).
Level-2A	- Bottom Of Atmosphere (BOA) reflectance - Include: Aerosol Optical Thickness (AOT), Water Vapour (WV), Scene Classification Map (SCM), Quality Indicators for cloud and snow probabilities at 60 m spatial resolution

the surface type. (ESA website and sentinel-3 handbook).

2.3.2 Sentinel-2

Sentinel-2 is an ESA, high-resolution multispectral imaging, polar-orbiting satellite mission which provides SPOT and LANDSAT image types data designed for seven years lifetime. The full Sentinel-2 mission includes twin satellites in the same orbit, Sentinel-2A, launched on 23 June 2015 and Sentinel-2B on 7 March 2017. Sentinel-2 carries a push-broom Multi-Spectral Instrument (MSI) payload with the aim of land cover change detection, agricultural applications, coastal zone, inland water and Glacier monitoring.

The sensor characteristics are a swath-width of 290 km Field Of View (FOV), Multispectral data with 13 bands (443-2190 nm) from VNIR to SWIR (Table 3.4), spatial resolution at 10 (four visible and near-infrared bands), 20 (six red-edge and shortwave infrared bands) and 60 m (three atmospheric correction bands), 5 days revisit, 12-bit radiometric resolution, sun-synchronous orbit at a mean altitude of 786 km. From five Sentinel-2 product types, Level-0, Level-1A products are not available, and Level-1B, Level-1C, and Level-2A products are available for users and listed in Table 2.6.

2.4 In situ methods

A primary requirement for satellite algorithms and validation is adequate set of radiometric, optical and chemical field measurements, so called match up in situ data. For instance, field data conducted in time and location of satellite overpass; in addition with a standard set of measurement protocols and guidelines to be accepted for the algorithm development and validation. These variables are classified as the radiometric measurements, IOPs, biogeochemical and bio-optical measurements, and ancillary data and metadata (which are necessary for support, analysis and quality control of other quantities) [113].

Table 2.7: Radiometric quantities for satellite system and product development and validation.

Radiometric Quantities	Required	Highly Desired	Specialized Measurement	Derived
Downwelled Irradiance	✓			
Upwelled Radiance	✓			
Upwelled Irradiance			✓	
Radiance Distribution in water			✓	
Water Surface Radiance in air		✓		
Incident Irradiance in air	✓			
Normal Solar Irradiance	✓			
Sky Radiance		✓		
Diffuse Sky Irradiance		✓		
Direct Sun Irradiance				✓
Water-Leaving Radiance				✓
Remote Sensing Reflectance				✓
Attenuation Coefficient				✓
BRDF*				✓
Aerosol Optical Depth	✓			
Aerosol Phase Function				✓
Absorbing Aerosol Height Profiles**			✓	

* Ocean Bidirectional Reflectance Distribution Function
**LIDAR Profilometer)

Table 2.7 displays a list of in situ radiometric quantities for the satellite ocean color sys-

Table 2.8: Optical properties for algorithms and IOP-based algorithm development and validation.

Inherent Optical Properties	Required	Highly Desired	Specialized Measurement	Derived
Beam Attenuation Coefficient		✓		
Absorption Coefficient		✓		
Backscattering Coefficient		✓		
Scattering Coefficient				✓
Volume Scattering Function			✓	
Particle Absorption Coefficient		✓		✓
Dissolved Material Absorption Coefficient		✓		
Non-Pigmented Particle Absorption Coef.		✓		
Phytoplankton Absorption Coefficient		✓		

tem and algorithm validation. Some quantities can also be derived from non-radiometric parameters (e.g., IOPs). For instance, Rrs can be derived from the ratio of $L_w(\lambda)/E_s(\lambda)$, or indirectly from the IOPs ratio $b_b(\lambda)/a(\lambda)$. Radiometric profiles such as upwelling radiance, $L_u(\lambda, z)$, downwelling irradiance, $E_d(\lambda, z)$, measurements of surface irradiance, $E_s(\lambda, 0^+)$ usually collected near-simultaneously either on the deck of the vessel or nearby buoy (e.g. surface incident spectral irradiance in air, $E_d(0^+, \lambda)$) are the fundamental quantities required for measuring normalized water-leaving radiances (L_{WN}), or Rrs. When available, other radiometric measurements listed in the Table 2.7 are related quantities for algorithms development programs.

To develop and validate semi-analytical algorithms, it is required to obtain optical quantities such as absorption $a(z, \lambda)$, beam attenuation $c(z, \lambda)$, and backscattering $b_b(z, \lambda)$ coefficients. In situ, or laboratory spectrophotometer or fluorimeters use to measure the filtered water sampled in different depth to drive the IOPS. Table 2.8 shows a list of IOPs required for algorithms and semi-analytical IOP based approaches. Pigments Concentration by High-Performance Liquid Chromatography [$mg\, m^{-3}$ or $\mu g\, L^{-1}$] and fluorometric methods and fluorometric-determined concentrations are used to measure the phytoplankton pigment Chl-a and the effects of other accessory pigments and water constitutes on water-leaving radiances. HPLC methods are more accurate than the fluorometric deter-

Table 2.9: In situ biogeochemical and bio-Optical properties of water measurements for bio-optical algorithm development and validation.

Biogeochemical and Bio-Optical Quantities	Required	Highly Desired	Specialized Measurement	Derived
Pigment Composition (HPLC method)	✓			
Chl-a Conc. (Fluorometric method)	✓			
Phycobiliprotein Concentrations			✓	
Coccolith Concentrations			✓	
Total Suspended Particulate Material (SPM)			✓	
Fluorescence Intensity, in situ profile		✓		
Coloured dissolved organic material			✓	

minations which often have a systematic error. However, fluorometric methods are simple and less costly which allow having a large number of samples at a region to be studied. Table 2.9 shows a list of bio-optical measurements required for bio-optical model assessment.

Ancillary data and metadata including environmental variables, geographical, and time information about each sampling station are necessary to add with the field data. Metadata such as longitude, latitude, date, and time, in addition to ancillary data including environmental conditions that effect the Lake state such as wind speed and direction, cloud cover, surface condition. Other ancillary measurements, for example, temperature, salinity, Secchi depth, depth profiles may require during each field measurements.

Table 2.10: Ancillary data and metadata required to support analysis and quality control of other in situ data.

Ancillary Data and Metadata	Required	Highly Desired	Specialized Measurement	Derived
Latitude and Longitude	✓			
Date and Time (UTC)	✓			
Wave Height	✓			
Whitecap Conditions		✓		
Wind Speed and Direction	✓			
Surface Barometric Pressure	✓			
Cloud Cover	✓			
Cloud Type		✓		
Secchi Depth	✓			
Water Depth	✓			
Conductivity and Temperature over Depth		✓		

Chapter 3

Evaluation of Sentinel-2 and Sentinel-3 Chlorophyll-a Products in the Western Basin of Lake Erie

3.1 Study area

Lake Erie is delimited to the north by Ontario, Michigan to the west, New York to the east, and Ohio and Pennsylvania to the south. It covers a surface area of 25,744 km (Table 3.1). Lake Erie is the warmest, shallowest and most biologically productive of the five Laurentian Great Lakes. It is the fourth largest in surface area yet smallest in water volume making it vulnerable to water level fluctuations [114,115]. This study focuses on the western basin of Lake Erie (Fig. 3.1).

Water depth and nutrient load are the two main factors that impact Chl-a concentration and lead to continuous blooms of green and blue-green algae in this Lake [116]. The western basin is the shallowest section of all the Great Lakes, with an average depth of 7.4m, receiving the majority of loaded nutrients, mainly nitrogen and phosphorus [116]. Three main rivers, the Maumee, Raisin and Detroit Rivers, feed Lake Erie. Although, the Detroit River is the primary inlet, contributing up to 90 % of the inflow into the lake,

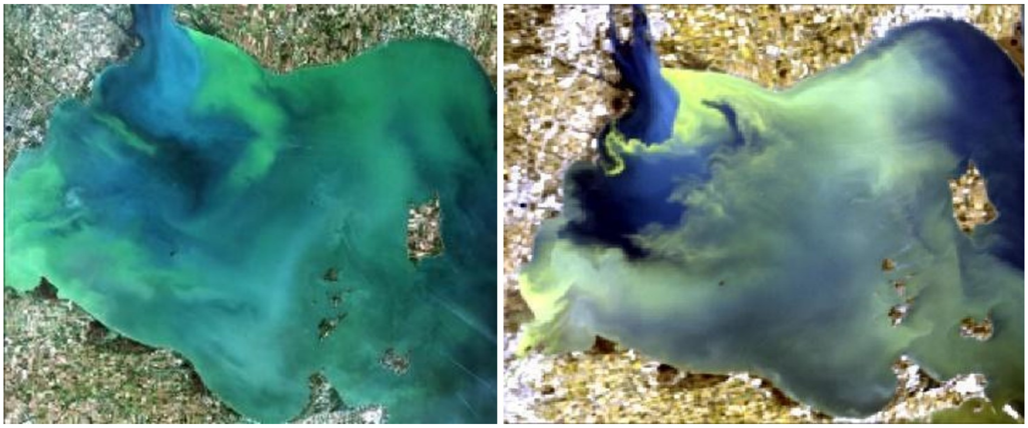

Figure 3.1: The study area, western Lake Erie. Left: Algal blooms in the lake acquired by Sentinel-2 on Oct. 2, 2017. Right: Sentinel-3 on Sep. 26, 2017.

Table 3.1: Lake Erie characteristics [2, 3].

Indication	Description
Group	Great Lakes
Location	42.011^o N, 81.015^o W
Max. depth	64 m
Max. length	388 km
Max. width	92 km
Mean elevation	174 m above sea level
Average depth	20 m
Basin countries	Canada , United States
Trophic status	Mesotrophic in the 1980s and early 1990s Eutrophic and hypereutrophic starting from the 2000s
Lake type	Glacial
Primary inlet	Detroit River
Outflows	Welland Canal, Niagara River
Surface area	25,874 km^2
Basin sections	West basin, Central basin, East basin, 7.4, 18.3, and, 24 m

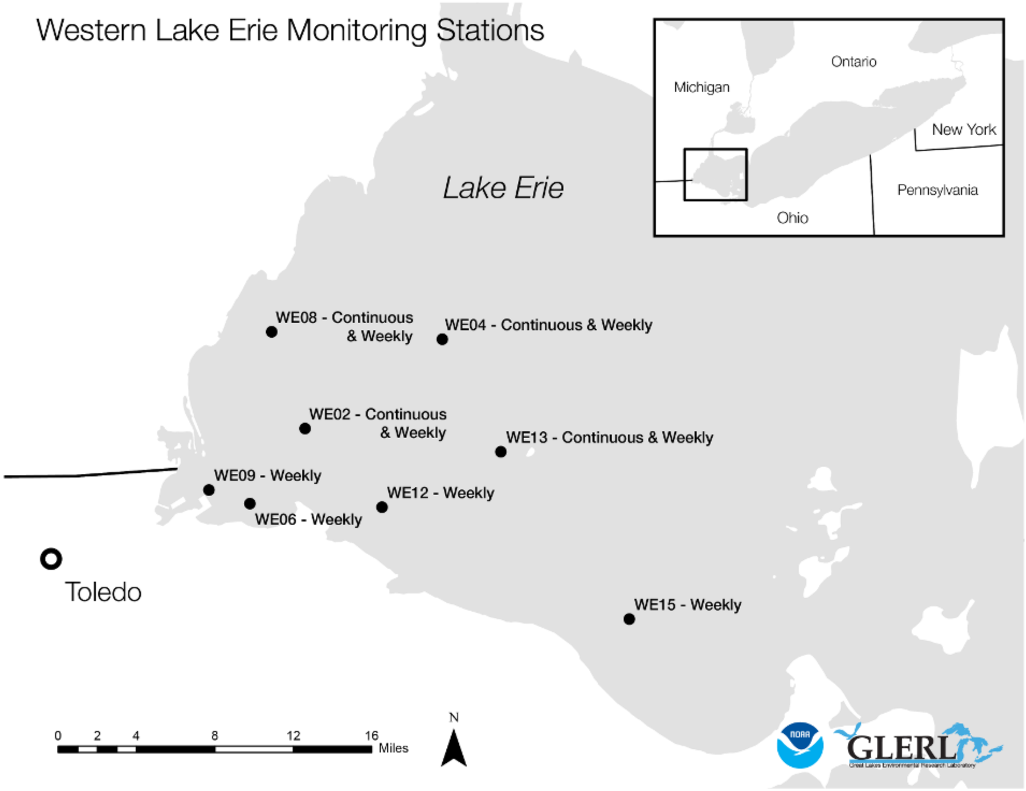

Figure 3.2: Western Lake Erie weekly and real-time monitoring stations.

the Maumee River loads nearly half of the nutrients into the basin [3]. This is because the Maumee River dominated by agricultural land area. Compared to the Detroit River (joining Lakes Huron and Erie) which is surrounded by industrial/urban, residential, and partially wood/grassland cover.

The annual nutrient loads occur in the spring, with the leading productivity in the summer. Since the mid-1990s, many studies have shown that summer blooms have increased in biomass and are contaminated by toxic cyanobacterium, Microcystis aeruginosa [117]. From 2002 to 2015, average yearly peak bloom magnitude in the western basin was 912 km^2 as the most massive blooms occurred in 2011 and 2015 [7, 118].

3.2 In-situ data

Since 2008, NOAA - Great Lakes Environmental Research Laboratory has conducted a comprehensive weekly water sampling program from May to October at the eight specific stations in surface and bottom depth (surface approximately 0.75 m, and 1 m off bottom of lake) in the western basin of Lake Erie (Fig. 3.2); with the aim of measuring phytoplankton biomass and its toxicity. The data are collecting on Chl-a concentration, nutrients, phycocyanin, dissolved microcystin, particulate microcystin, secchi depth, and water temperature sampled from a CTD (conductivity, temperature, and depth) profiler [119].

In addition to weekly monitoring, real time monitoring continuously are measuring parameters such as air temperature, water temperature, barometric pressure, wind speed, wind direction, turbidity, Chl-a, phycocyanin, Dissolved Oxygen (DO), pH, depth, and nitrogen (NO3) every 15 minutes at 4 fixed moorings (Fig. 3.2).

Environmental Sample Processor (ESP) which is used to tracking the toxicity of blue-green algae also collects water samples to track microcystin, the common cyanobacteria toxin in this area providing NOAA's twice-weekly Lake Erie HAB Bulletin and the Experimental HAB Tracker nowcast and five-day forecast to make available information for water managers with the bloom location, severity and toxicity [119].

We used the weekly Chl-a data measurements from May-October 2017 match with Sentinel-3A, and 2016 and 2017 for Sentinel-2A overpass. The data were selected to match (±3 days window) the image acquisition date. Table 3.2 shows the image acquisition dates corresponding with filed sampling dates for both Sentinel-2A and Sentinel-3A satellites.

3.3 Remote sensing data

Sentinel-3A OLCI Level-1 NRT FR 2017 images were downloaded from Sentinel-3 Pre-Operations Data Hub (https://scihub.copernicus.eu/s3). Level-1 products provide TOA radiances in the VIS-NIR bands (Table 3.3). Twelves Cloud free images were available match up with the in situ data (Table 3.2). Sentinel-2 Level-1C images were downloaded

Table 3.2: Date of acquisition imagery and water sample acquisition of Sentinel-3A and Sentinel-2A used in this study.

Sentinel-3A		Sentinel-2A	
Filed date	Image date	Field date	Image date
5/8/2017	5/7/2017	6/26/2017	6/24/2017
5/30/2017	5/30/2017	7/11/2017	7/9/2017
6/12/2017	6/11/2017	7/30/2017	7/29/2017
6/26/2017	6/26/2017	10/2/2017	10/2/2017
7/17/2017	7/16/2017	7/18/2016	7/20/2016
7/31/2017	7/30/2017	8/7/2016	8/9/2016
8/7/2017	8/7/2017	8/29/2016	8/29/2016
8/14/2017	8/14/2017		
8/28/2017	8/26/2017		
9/25/2017	9/26/2017		
10/10/2017	10/8/2017		
10/16/2017	10/16/2017		

from Sentinels Scientific Data Hub. Cloud free images were available on 24 June, 9 and 29 July, 2 October (2017), 18 July, 9 and 29 August (2016) (Table 3.2). Level-1C products are provided in TOA atmosphere reflectance in cartographic geometry with all parameters to transform them into radiance and the granules (called tiles, $100 \times 100\ km^2$ ortho-images in UTM/WGS84 projection). These data are acquired in 13 spectral bands (Table 3.4).

3.4 Baseline algorithm

We used Baseline algorithm which exploit the height of the fluorescence and maximum scattering peak of Chl-a above a baseline, which passes through two other spectral bands outside of the peak. The general equation of a baseline algorithm is the line hight (Eq. 3.1):

$$Line\ Height = L_2 - L_1 - (L_3 - L_1)\frac{(\lambda_2 - \lambda_1)}{(\lambda_3 - \lambda_1)} \tag{3.1}$$

Where the indices 1 and 3 indicate the baseline bands and index 2 the peak or signal

Table 3.3: Sentinel-3 (OLCI) bands specification [4].

Band No.	λ center	Bandwidth	Function
Oa1	400	15	Aerosol correction, water constituent retrieval
Oa2	412.5	10	Yellow substance and detrital pigments
Oa3	442.5	10	Chl absorption max., biogeochemistry
Oa4	490	10	High Chl, other pigments
Oa5	510	10	Chl, sediment, turbidity, red tide
Oa6	560	10	Chl reference
Oa7	620	10	Sediment loading, Phycocyanin
Oa8	665	10	Chl, sediment, yellow substance, vegetation
Oa9	673.75	7.5	For improved fluorescence retrieval
Oa10	681.25	7.5	Chl fluorescence peak
Oa11	708.25	10	Chl fluorescence baseline
Oa12	753.75	7.5	O2 absorption, clouds, vegetation
Oa13	761.25	2.5	O2 absorption band/aerosol corr.
Oa14	764.375	3.75	Atmospheric correction
Oa15	767.5	2.5	O2A for cloud top pressure, fluorescence
Oa16	778.75	15	Atmos. corr. ,aerosol corr.
Oa17	865	20	Atmos. corr. ,aerosol corr., clouds
Oa18	885	10	Water vapour absorption ref. band
Oa19	900	10	Water vapour absorption, vegetation
Oa20	940	20	Atmos./ aerosol corr.
Oa21	1020	40	Atmos./aerosol corr.

Table 3.4: Sentinel-2 spectral band characteristics.

Sentinel-2 Bands	Central Wavelength (nm)	Bandwidth (nm)	Spatial Resolution
B1- Coastal aerosol	443	20	60
B2- Blue	490	65	10
B3- Green	560	35	10
B4- Red	665	30	10
B5- Vegetation Red Edge	705	15	20
B6- Vegetation Red Edge	740	15	20
B7- Vegetation Red Edge	783	20	20
B8- NIR	842	115	10
B8a- Vegetation Red Edge	865	20	20
B9- Water Vapour	945	20	60
B10- SWIR Cirrus	1380	20	60
B11- SWIR	1610	90	20
B12- SWIR	2190	180	20

band. This algorithm used by Gower, 2003, [100] and was characterized for MERIS toolbox. However, the algorithm applied in the FLH/MCI processor in Sentinel Application Platform (SNAP) contains an additional factor to correct the influence of thin clouds using K=1.005 (Eq. 3.2).

$$Line\ Height = L_2 - K * [L_1 + (L_3 - L_1)\frac{(\lambda_2 - \lambda_1)}{(\lambda_3 - \lambda_1)}] \tag{3.2}$$

Figure 3.3 (a) displays fluorescence height over a baseline, where the phytoplankton Chl-a fluorescence at 680.5 nm and its height above a baseline through the measurements at around 664nm and 750 nm is calculated [9] And, figure 3.3 (b) displays overlapping of fluorescence and elastic radiance peaks in NIR for two [Chl] values [100].

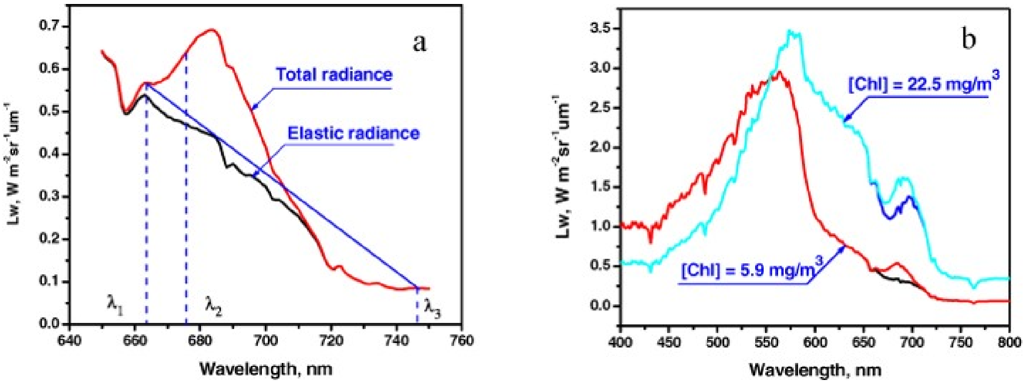

Figure 3.3: (a) Fluorescence height over baseline, (b) Overlapping of fluorescence and elastic radiance peaks in NIR for two [Chl] values [9].

3.5 Methodology

3.5.1 Image processing

Sentinel-3A

Sentinel-3 Toolbox (S3TBX) version 6.0.0 in the Sentinel Application Platform (SNAP) on Windows 10 (64 bit) was used to process the images. Images were subset to a geographic region bounded by the latitude and longitude to limit the lake of interest. The conversion from TOA radiance (LTOA) to TOA reflectance (RTOA) was done in SNAP Data Processors to be further analyzed.

The conversion from TOA radiance (LTOA) to TOA reflectances (RTOA) done through SNAP Data Processors - Radiance-to-Reflectance Processor. This conversion aims to extract the pixel Level-1B data and convert the included radiance into reflectance through three main steps. First, Pre-processing for geometry and meteorological parameters (etc., pressure, wind) at each pixel. Second, pixel identification: starts with reading of the INVALID flag, if it is set to TRUE, no further processing of the current pixel is performed, and the next pixel is examined. Otherwise, processing of the current pixel is pursued. And third, Pixel extraction and reflectance conversion. Figure 3.4 displays the diagram of Radiances into Reflectances Conversion.

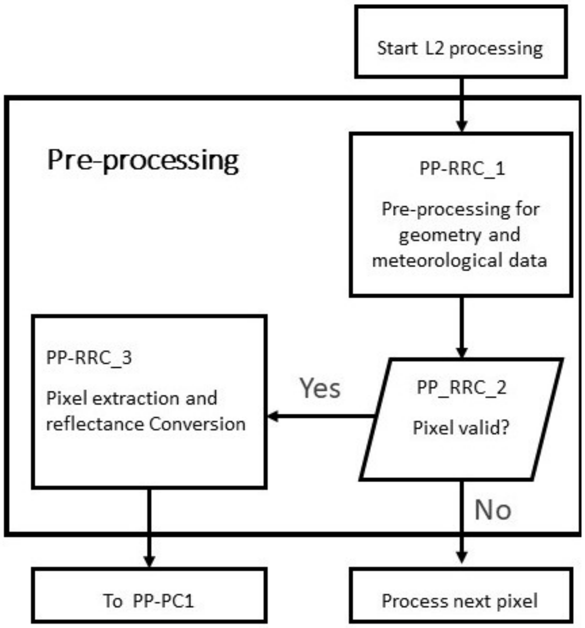

Figure 3.4: Diagram of Radiances Into Reflectances Conversion processes [10].

Thematic water processing using FLH/MCI Processor was performed to extract MERISFLH and MERISMCI signals. The FLH/MCI processor can be invoked in the Sentinel Toolbox from tool menu by selecting Processing Thematic Water Processing, FLH/MCI Processor. We defined a new red-edge peak height band combination, by the Processor and named it S3FLH. We were able to develop this new algorithm because, in the FLH/MCI processor the baseline bands and the signal band are freely configurable. Two different signal bands, 709nm and 681nm, with different baseline bands (665, 673, 753 nm) were configured to calculate MERISFLH, MERISMCI, and S3FLH. Table 3.5 shows the different band combination selected for each product. Level-1 MCI/FLH products are calculated from the TOA radiance which has the units of $mWm^{-2}nm^{-1}sr^{-1}$ whereas the L2 MCI/FLH products are derived from water-leaving reflectance which is dimensionless.

Cloud-free pixel values corresponding to the location of each sampling station were extracted from each thematic product to be evaluated with the ground data. To extract the MCI and FLH indices from the images at locations specified in a point feature class,

Table 3.5: The signal and baseline bands used in the OLCI Chl-a retrieval products.

	Sentinel-3 bands (nm)				
Product	665	673	681	709	753
MERISFLH	λ_1		λ_2	λ_3	
S3FLH		λ_1	λ_2	λ_3	
MERISMCI			λ_1	λ_2	λ_3

we used the Extract Multi Values to Points tool with Arc GIS. Each pixel which covered the geographic location of the station value extracted for each input raster, and a new field containing the cell values for each input raster added to the input point feature class. Then an attribute table exported to Microsoft Excel to establish a relationship between the radiometric indices and in-situ Chl-a content, and assessment of created models. Figure 3.5 displays an overview of the methodology applied in this research.

Sentinel-2A

Sentinel-2 Toolbox (S2TBX) version 6.0.0 in Sentinel Application Platform (SNAP) on Windows 10 (64 bit) was used to process the images. Sentinel-2 is delivered with three spatial resolution options. The spatial resolution of Sentinel-2 is dependent on the particular spectral band. Level1C Sentinel-2 data includes the RBG-NIR as 10m bands and SWIR as 20m bands. As SNAP feature is not supported for a multi-size product we needed to upscale the RGB-NIR bands to 20m and resample them with the rest of the 20m bands. Spatial subset of data created by given pixel positions using subset operator. Sentinel-2 MCI Processor was used to calculate the MCI, which calculates the MCI by exploiting the height of a measurement over a specific baseline. We configured the suited band combination on Sentinel-2 MSI images (a signal band at 705nm above the baseline passing through 665 nm and 740nm bands) to exploit the height of a maximum Chl-a peak.

Pixel values were extracted from each sampling location to correlate with in situ Chl-a measurements. To extract the indices from raster images to a table, we used Arc GIS spatial analysis tools by extracting the values of each pixel which covered the geographical

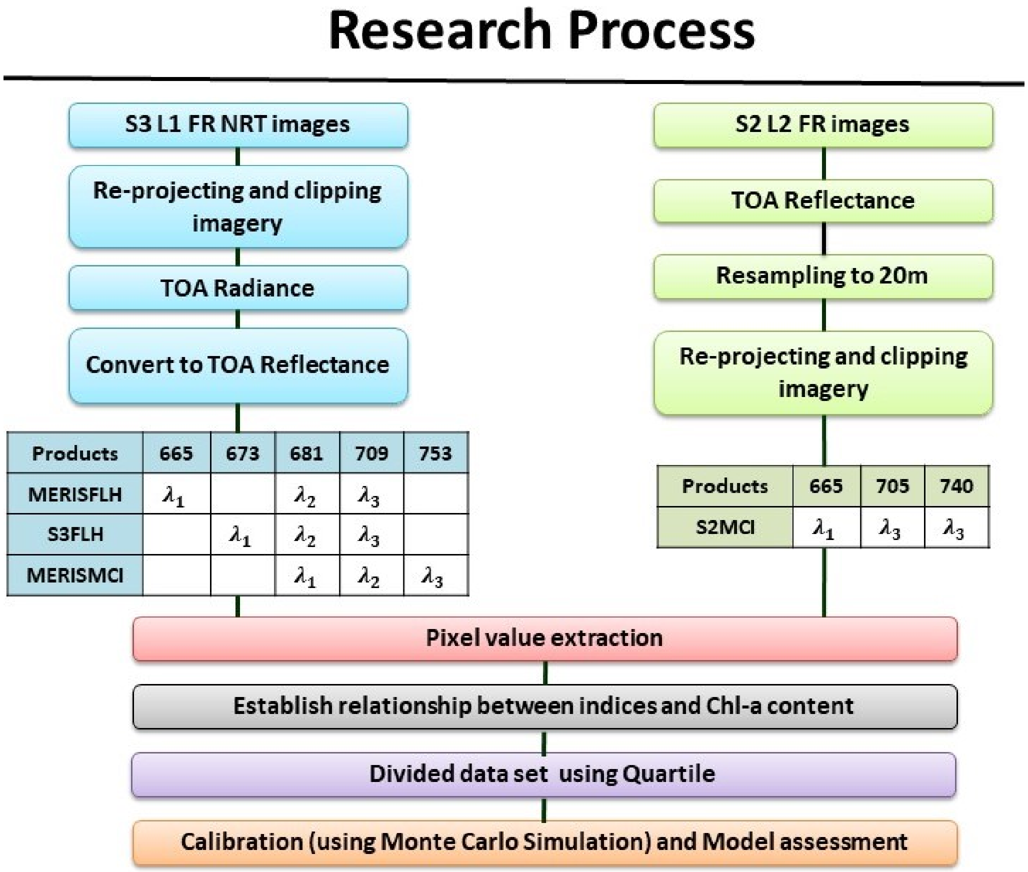

Products	665	673	681	709	753
MERISFLH	λ_1		λ_2	λ_3	
S3FLH		λ_1	λ_2	λ_3	
MERISMCI			λ_1	λ_2	λ_3

Products	665	705	740
S2MCI	λ_1	λ_3	λ_3

Figure 3.5: Processing flowchart of Sentinel-3A OLCI and Sentinel-2A MCI images to retrieve Chl-a indices related to in-situ Chl-a Concentration .

location of the station value, and then registering the values in an attribute table of a predefined point layer. Finally, a CSV-file format exported as an output to establish a model between the extracted indices and Chl-a contents.

3.5.2 Model assessment

Dataset Generation

The retrieval values from three products, MERISMCI, MERISFLH, S3FLH and the match up in situ data were combined as a dataset to be used for the algorithms calibration. Figure 3.6 displays the flowchart of the steps of separating dataset using Quartile method for calibration and testing the constructed models for Sentinel-3 and Sentinel-2 data.

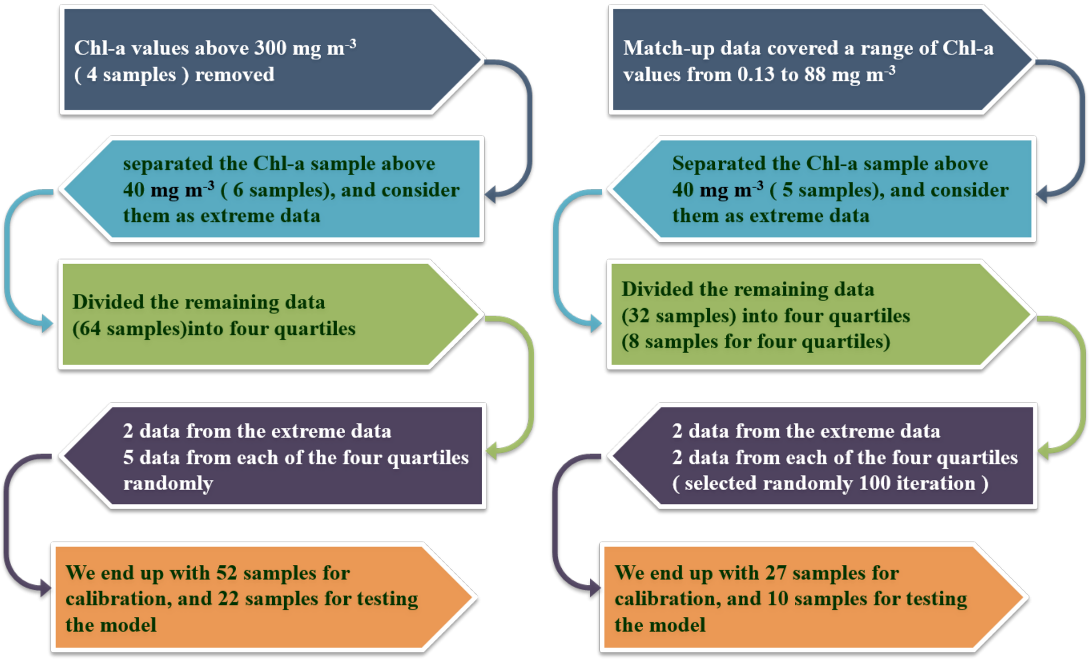

Figure 3.6: Flowchart of the separate dataset and generation database from Sentinel-2A (right figure) and Sentinel-3A OLCI algorithms retrieval values (left figure) and match up in-situ Chl-a concentration using Quartile method for model assessment.

For Sentinel-3A, Chl-a values above 300 mgm^{-3} (4 samples) removed from the data set due to the uncertainty of the data quality and their effects on model performance. Some of the optical sensors showed signal saturation over high phytoplankton biomass [120,121], possibly eliminating extremely high biomass from analyses. Moreover, the Chl-a and MCI indices correlation is documented to move to saturation at Chl 300 μgL^{-1} [120]. Since the Chl-a data (74 samples) are not symmetrically distributed, we separated the Chl-a sample above 40 mgm^{-3} (6 samples), and consider them as extreme data. This decision reflects that the large portion of the Chl-a values are below $40mgm^{-3}$. We then divided the remaining data into four quartiles. We selected two data from the extreme data, and five data from each of the four quartiles randomly. As a result we end up with 52 samples for calibration, and 22 samples for testing the constructed model [122].

The indices values from S2MCI product and the match up in situ data were combined as a dataset to be used for the algorithm calibration (Figure 3.6). The dataset split in 5 samples for extreme data (Chl-a sample above 40 mgm^{-3}), 8 samples for four quartiles (32 samples). We selected two samples from the extreme dataset and two samples from each quartile randomly iterating 100 times. The dataset divided into 27 sample for calibration and 10 sample for validation.

3.5.3 Calibration and validation

Sentinel-3A

Monte Carlo Simulation in MATLAB was used to calibrate the models (Figure 3.7). Monte Carlo simulation is a technique used to study how a model responds to randomly generated inputs. In this process, 30 samples randomly selected from the dataset of 52 are used to build the equations with a linear regression between Chl-a and the product retrieval values iterating 1000 times. The results are recorded for 1000 equation and the R2, slope, and intercept associated with each.

Then an R2 histogram created from all the recorded R2 to identify equations with the most frequent range of this coefficient. We plot the coefficients (slope, intercept) of the

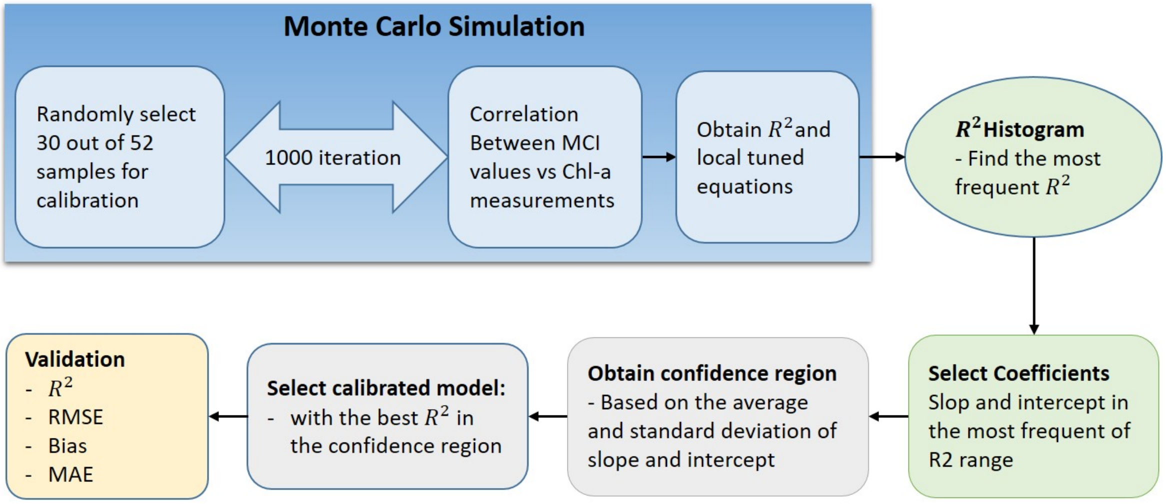

Figure 3.7: Monte Carlo calibration and validation scheme.

identified equations to obtain a confidence region (Figure 3.10). The calibrated model was selected with the best R2 in the confidence region based on mean and standard deviation. Then we validated the equation with 22 test data.

Sentinel-2A

The same calibration and validation process was carried out for the S2MCI indices and match up in situ dataset generated (Figure 3.6). In this process, 15 samples randomly selected from the dataset of 27 are used to build the equations with a linear regression between Chl-a and the product retrieval values iterating 1000 times.

The results are recorded for 1000 equation and the R2, slope, and intercept associated with each. Then an R2 histogram created to obtain the most frequent R2 from all the recorded R2 to identify equations with the most frequent range of this parameter. We plotted the coefficients (slope, intercept) of the identified equations with the most frequent R2 and created the confidence region (Figure 3.10). The calibrated model was selected with the best R2 in the confidence region based on mean and standard deviation. Then we validate the equation with 10 test data. Figures 3.9 and 3.10 are the R2 histograms

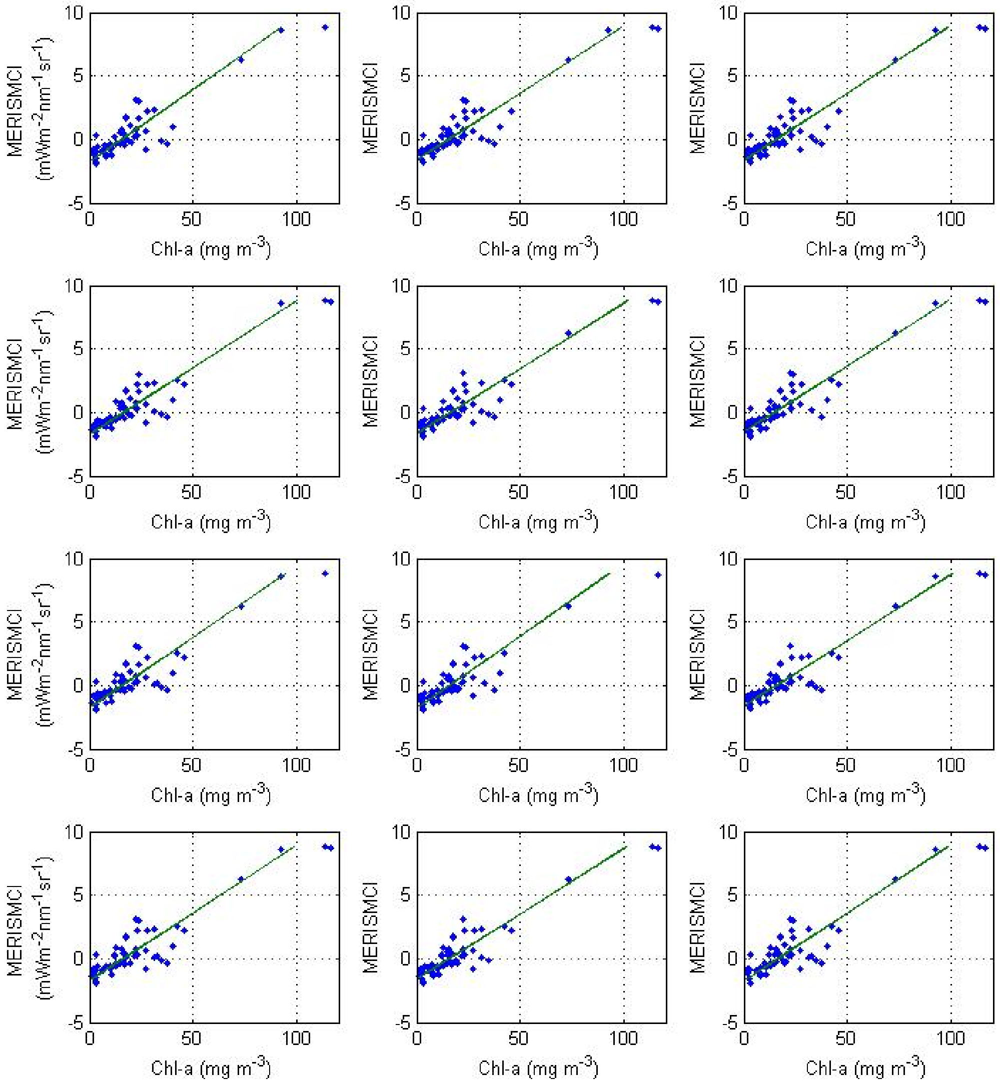

Figure 3.8: 12 out of 1000 calibration samples for MERISMCI algorithm.

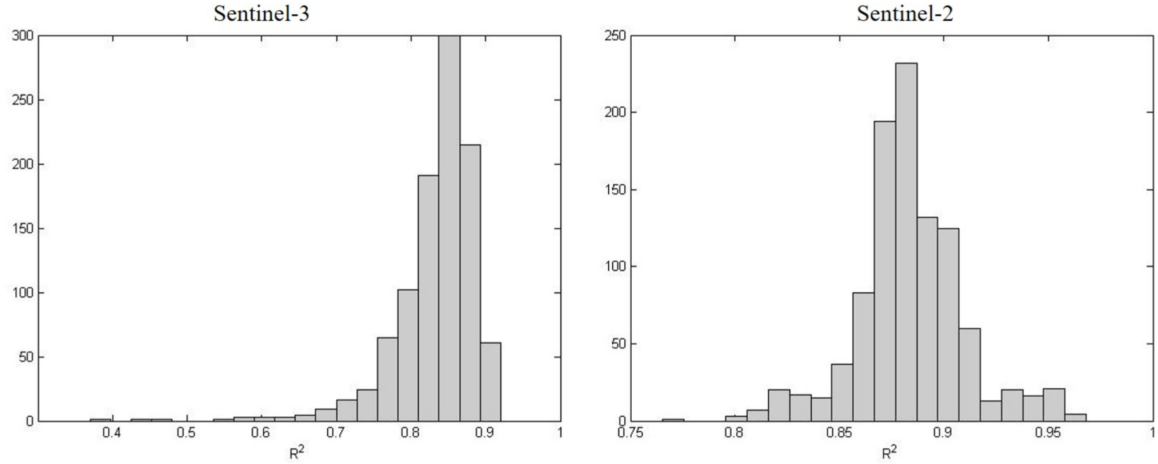

Figure 3.9: Histograms of the R^2 distribution for MERISMCI and S2MCI algorithms.

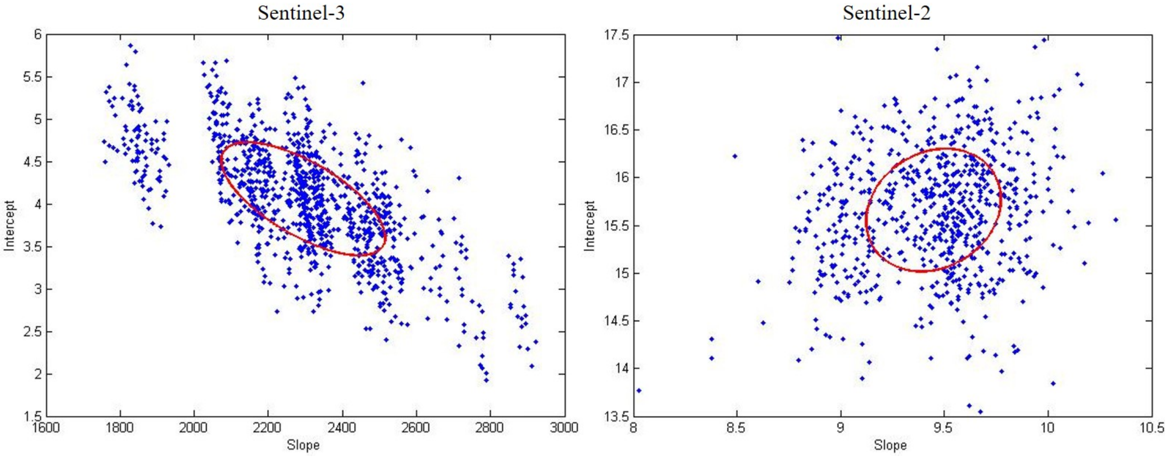

Figure 3.10: Plot of the slope vs intercept.

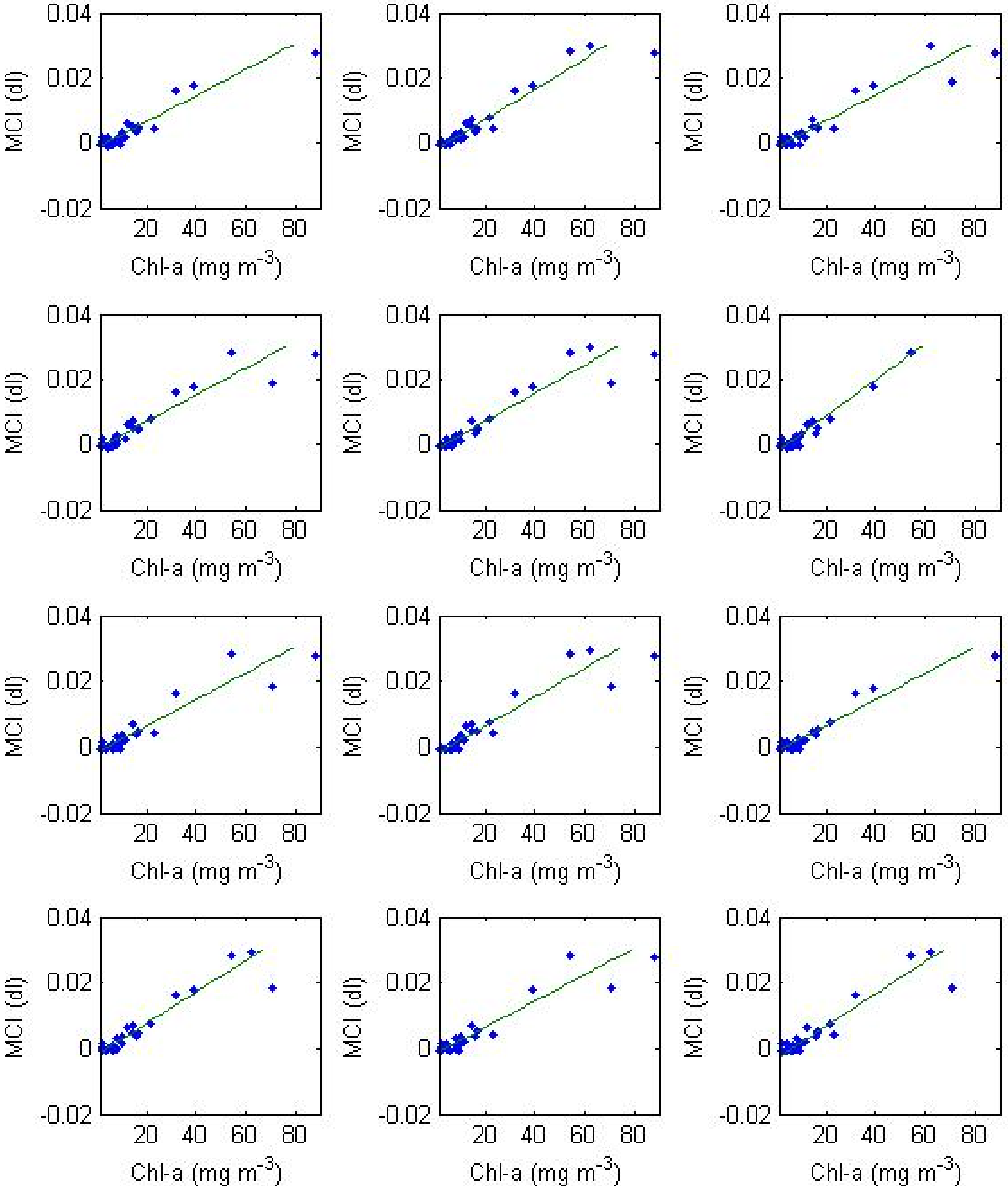

Figure 3.11: 12 out of 1000 calibration samples for S2MCI (Sentinel-2) algorithm.

and confidence region plots from the model assessment process.

3.5.4 Statistical Analysis

Statistical analysis was carried out to evaluate the uncertainty in satellite-derived estimates. Following estimators were used to comparison between in-situ measured and satellite derived estimates: R2 coefficient, Root Mean Square Error (RMSE), Bias, and Mean Absolute Error (MAE). Table 3.6 shows the formulation of these metrics.

Table 3.6: The error metrics for the model assessments.

Error metric	Equation	Error metric	Equation
R^2	$1-\frac{\sum(e_i)^2}{\sum(y_i-\overline{y})^2}$	Bias	$\frac{1}{n}\sum(e_i)$
RMSE	$\sqrt{\frac{1}{n}\sum(e_i)^2}$	MAE	$\frac{1}{n}\sum\lvert e_i\rvert$

3.6 Results and discussion

3.6.1 In-situ data

Table 3.7 presents the basic descriptive statistics of Chl-a measurements and confirms the complexity of optical properties of the waters being measured in western Lake Erie over summer 2017. N is the number of samples collected, and Std is standard deviation. In this study, the three models were evaluated for Chl-a less than 300 $mg\ m^{-3}$ with a range of 1.28 to 116 $mg\,m^{-3}$ with a mean value of 19.66 $mg\ m^{-3}$. Figure 3.12 displays the monthly variation of all weekly Chl-a measurements. The dataset is representative of a broad range of Chl-a concentrations. Overall, the level of Chl-a increases gradually over the months, showing the lowest values in May and highest in August and September.

Table 3.8 shows the summary of basic descriptive statistics of measured Chl-a concentration of the waters being measured in 24 Jun, 9 and 29 July, October 2th in 2017 and

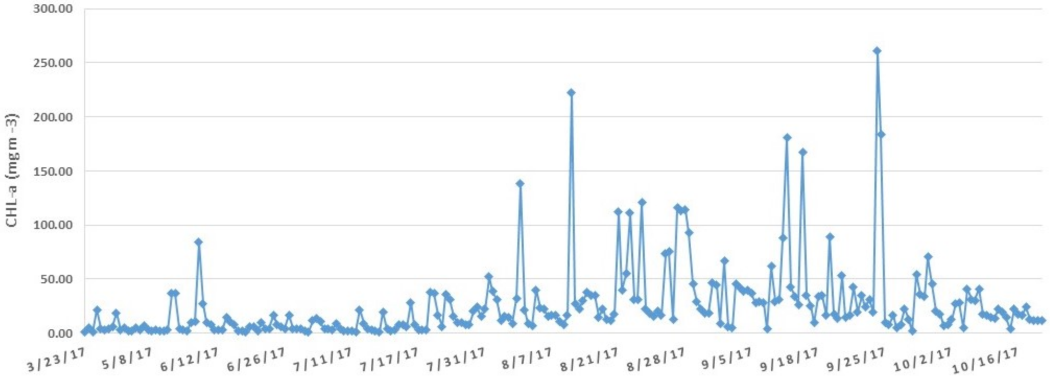

Figure 3.12: Time series of measured Chl-a obtained from NOAA-GLERL (May to October 2017).

Table 3.7: Descriptive statistic of Chl-a measurements match up with Sentinel-3 satellite overpass acquisition times for western Lake Erie over summer 2017.

	N	Min	Max	Mean	Median	Std
Chl-a	74	1.28	116	19.66	14.8	22.16

Table 3.8: Descriptive statistic of Chl-a measurements match up with Sentinel-2 satellite overpass acquisition times for western Lake Erie over summer 2016 and 2017.

	N	Min	Max	Mean	Median	Std
Chl-a	37	0.13	88	16.5	9.2	20.7

18 July, 9 and 29 August 2016 in Western Lake Erie match up with the Sentinel-2 image acquisition dates. In this study we evaluate the L2 S2MCI product for the data with a range of 0.13 to 88 $mg\ m^{-3}$ with a mean value of 16.5 $mg\ m^{-3}$.

3.6.2 Model Assessment

We used in situ Chl-a measurements to analyze the performance of FLH and MCI algorithms based on Sentinel-3 spectral bands. Figure 3.13 and Figure 3.14 display the retrieval of the fluorescence and scattering components from the Sentinel-3 images correlated with Chl-a and Log Chl-a . Three bands are utilized for each of the three algorithms to compute FLH and MCI (Table 3.5). The bands are 665, 681, and 709nm for MERISFLH [65] and 681, 709 and 753nm for MERISMCI [90]. An additional Sentinel-3 band exists at 673nm; thus we configured 673, 681, and 709nm and named it S3FLH algorithm. Table 3.9 and Table 3.10 presents local tuned equations, R^2, and RMSE for the three Sentinel-3 products. Figure 3.15 shows the correlation between FLH and MCI indices and Log Chl-a in a range 10 - 120 mg m-3.

Table 3.9: Equations and performance of Chl-a model for Sentinel-3A.

Model	Locally tuned equation	R^2	RMSE
MERISMCI Rad.	Chl-a $= 8.9\ MCI + 15.98$	0.82	8.86
S3FLH Rad.	Chl-a $= -34.6\ MCI + 18.3$	0.76	10.8
MERISFLH Rad.	Chl-a $= -15.4\ FLH + 13.8$	0.79	10.1
MERISMCI Ref.	Chl-a $= 2548\ MCI + 13.3$	0.67	12.7
S3FLH Ref.	Chl-a $= -9464\ MCI + 20$	0.54	15
MERISFLH Ref.	Chl-a $= -5292\ FLH + 18$	0.77	10.5

The result of FLH and MCI products in Level-2 processing, which is the normalized FLH and MCI, showes lower performance compared to the processing of Level-1 products. This normalization included pre-processing of geometrical and meteorological parameters (such as wind and pressure, bidirectional effects) at each pixel, pixel screening to find the

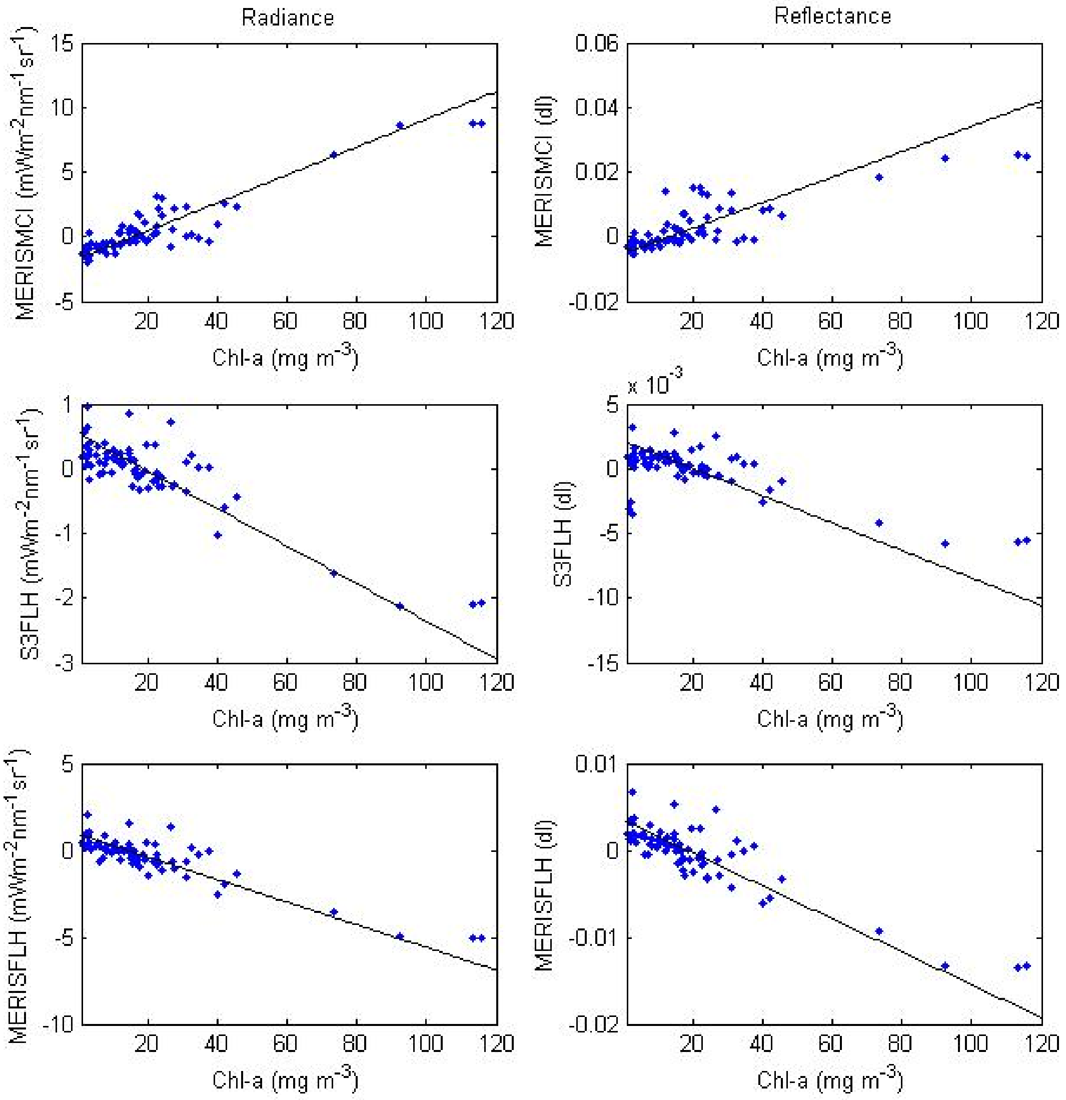

Figure 3.13: Correlation between FLH and MCI indices and in situ Chl-a using Sentinel-3 bands in TOA radiance and TOA reflectance.

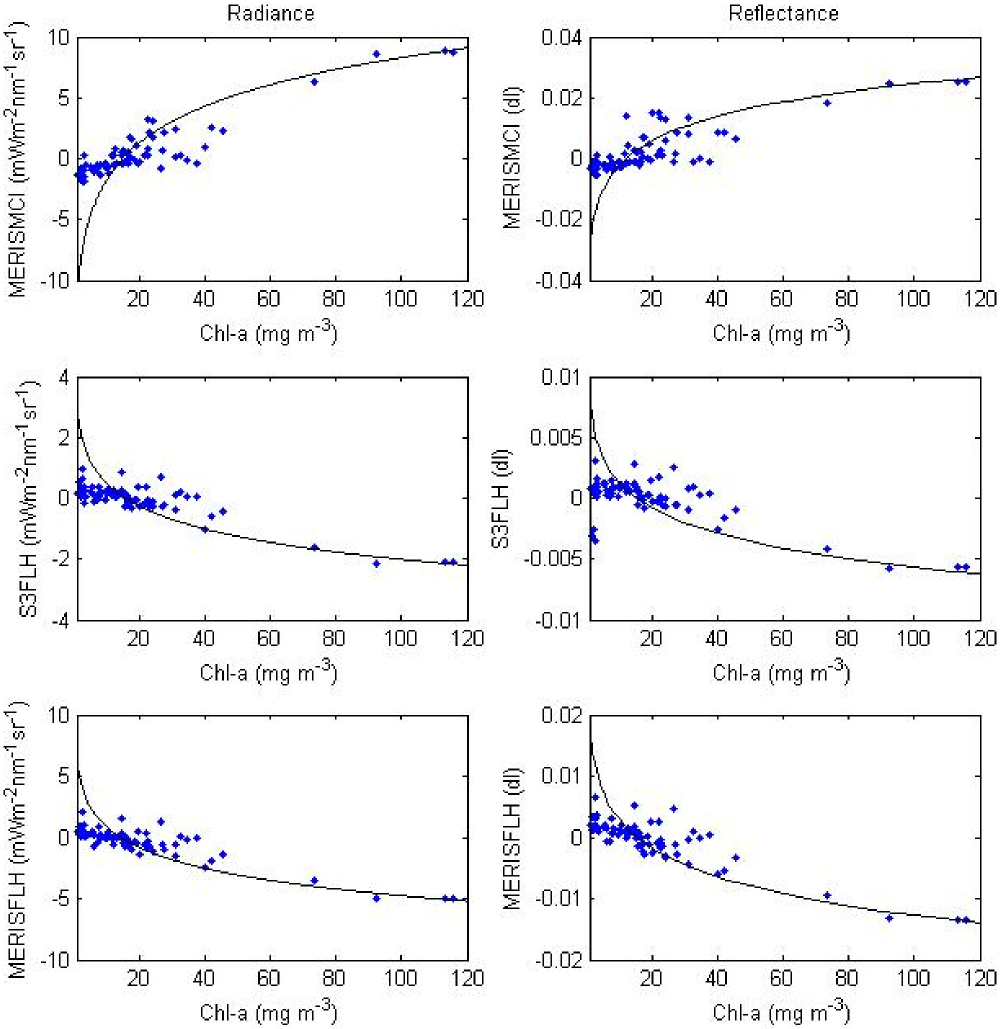

Figure 3.14: Correlation between FLH and MCI indices and Log Chl-a using Sentinel-3 bands in TOA radiance and TOA reflectance.

Table 3.10: Equations and performance of Log Chl-a model for Sentinel-3A.

Model	Locally tuned equation	R^2	RMSE
MERISMCI Rad.	MCI $= 4.38\, log(Chl - a) - 11.9$	0.83	8.4
MERISMCI Ref.	MCI $= 0.01\, log(Chl - a) - 0.02$	0.76	10.1
S3FLH Rad.	FLH $= -1.08\, log(Chl - a) + 3.0$	0.81	9.01
S3FLH Ref.	FLH $= -0.003\, log(Chl - a) + 0.008$	0.67	12.3
MERISFLH Rad.	FLH $= -2.42\, log(Chl - a) + 6.41$	0.82	8.5
MERISFLH Ref.	FLH $= -0.007\, log(Chl - a) + 0.02$	0.80	8.5

valid pixel, and conversion of the radiance signal to reflectance). The lower performance of normalized FLH and MCI radiances might be related to the poor pixel identification during the process of pixel flagging, which is affected by the complexity of the water and atmosphere condition.

MERISFLH using 665, 681, and 754nm performed better in comparison to the band combination of 673, 681, and 754 (S3FLH); this finding might be related to the closer positioned 673 nm proximate to 681nm, which makes the baseline a less accurate replacement of the elastic radiance (with the baseline) compared to the other band combinations. This sensitivity of the proximity of the band selection for FLH products in case 2 waters is not seen in the case 1 waters due to the low water constituents influences on the elastic radiance reflectance in the red spectral region. Nevertheless, despite their correlation of $R^2 = 0.79,\ 0.76$ in both algorithms, MERISFLH and S3FLH respectively, the results could be biased and not applicable for the lake type studied. In Figure 3.13 for the FLH band configurations, the FLH is positively correlated with Chl-a values up to 8 $mg\ m^{-3}$; however, at the higher Chl-a concentration, the FLH values become rapidly negative. This behavior is strongly due to the shift of the reflectance peak to the longer wavelengths along with the increase in [Chl-a] values [123].

As discussed in Chapter 2, FLH algorithms have proven to be applicable to ocean and oligotrophic waters where the Chl-a concentration is less than 10 $mg\ m^{-3}$. This limitation is due to the replacement of elastic reflectance to the baseline between λ_1 and λ_2 which deviate (associated with the cell scattering) from the flat line with increasing Chl-a amounts. However, in the low Chl-a concentrations the baseline nearly matches to the elastic reflectance in the red region.

MERISMCI products have been shown as a useful tool for monitoring algal blooms in optically complex waters (discussed in Chapter-2) [120]. In this study with a [Chl-a] range 0.1-300 $mg\ m^{-3}$, this product presented the best performance, for both L1 and L2 products processed compared to FLH products. The retrieved MCI showed a strong linear correlation with the Chl-a measurements ($Chl - a = 8.9\ MERISMCI + 15.98$, $R^2 = 0.82$, and $RMSE = 8.86$), (Table 3.9). Binding et al. [124] investigated a comprehensive evaluation of all Chl-a MERIS products and determined the MCI to be a more effective algorithm for eutrophic conditions. They also studied [120] the assessment of MCI for waters ranging from optically complex to low Chl-a conditions. Their results showed the MCI algorithm to be a useful tool in algae monitoring with Chl-a range of 10-300 $mg\ m^{-3}$. In our study, also in agreement with [120, 124], the MCI values are negative or negligible for almost Chl-a$<$ 20 $mg\ m^{-3}$, meaning that there was no reflectance in the peak 709 nm and following Chapter-2 discussion, the peak should be shifted to the shorter wavelengths for could capture by FLH products at 681nm. Moses et al. [125] suggest the threshold of 10 $mg\ m^{-3}$ for MCI application. Gower et al. [94] noted the applicability of the MCI algorithm for Chl-a concentration above 30 $mg\ m^{-3}$. We tuned the equation for Chl-a values $> 30\ mg\ m^{-3}$. Subsequently, the MCI showed a strong correlation with $R^2 > 0.91$.

L2S2MCI with the combination of 665, 705, 740nm to compute the MCI from the Sentinel-2 images, showed a very good correlation with the in situ Chl-a data in the studied stations ($Chl - a = 2158\ S2MCI + 3.9,\ R^2 = 0.92$) . Figure 3.16 displays correlation between S2MCI and in-situ Chl-a. The sensor has the advantage of higher spatial resolution (10, 20m) compared to Sentinel-3 OLCI instruments (300 m), which make it useful for monitoring small lakes [126]. Water constituents are varied spatially even within a few meters and within a short period; for instance, during the raining season loading a mass of particulate and dissolved matters discharge into the water body. Kutser [127] studied the extent of blue-green algae using different satellite sensors. The result noted the limitation

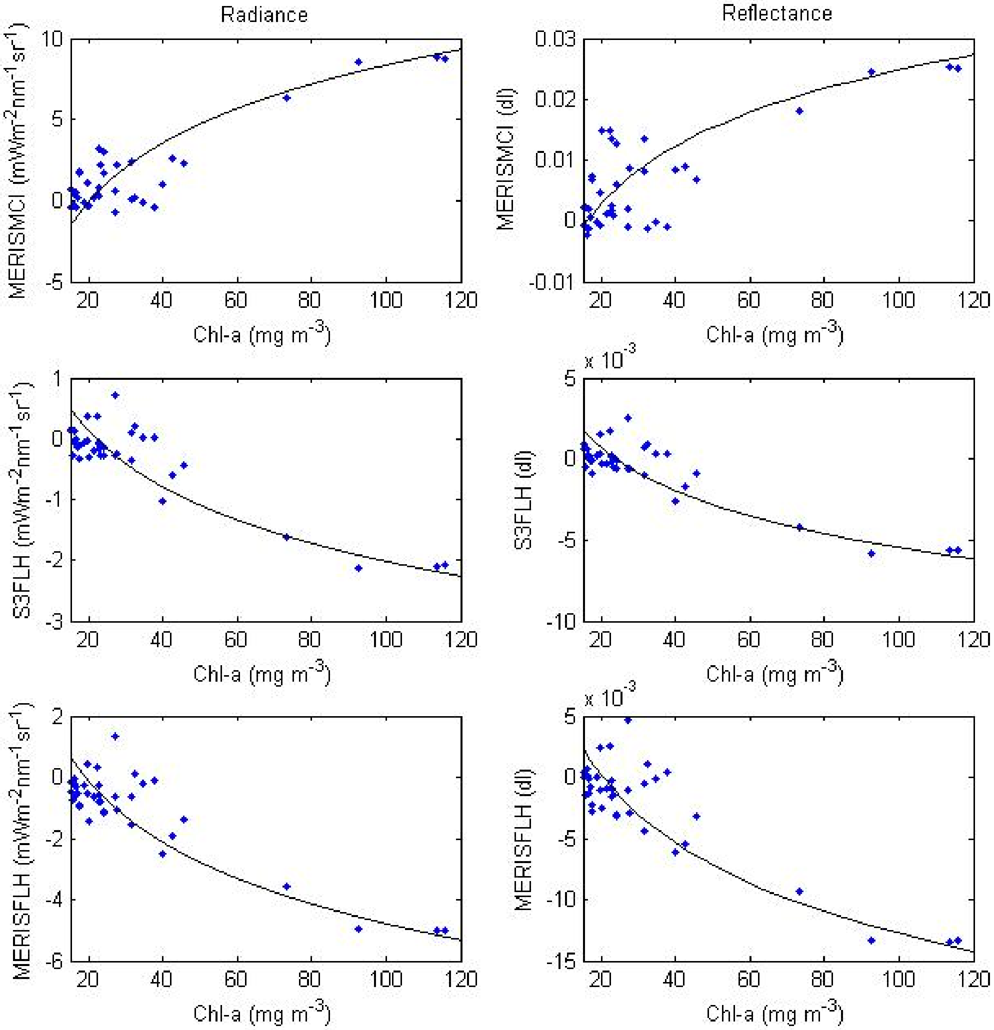

Figure 3.15: Correlation between FLH and MCI indices and Log Chl-a (10 - 120 mg m-3) using Sentinel-3 bands in TOA radiance and TOA reflectance.

Table 3.11: Equations and performance of Log Chl-a (10 - 120 mg m-3) model for Sentinel-3A.

Model	Locally tuned equation	R^2	RMSE
MERISMCI Rad.	MCI $= 5.24\, log(Chl - a) - 15.8$	0.87	8.4
MERISMCI Ref.	MCI $= 0.014\, log(Chl - a) - 0.038$	0.76	11.8
S3FLH Rad.	FLH $= -1.33\, log(Chl - a) + 4.09$	0.87	8.1
S3FLH Ref.	FLH $= -0.004\, log(Chl - a) + 0.012$	0.87	8.2
MERISFLH Rad.	FLH $= -2.88\, log(Chl - a) + 8.49$	0.88	7.8
MERISFLH Ref.	FLH $= -0.008\, log(Chl - a) + 0.024$	0.87	8.1

of these sensor spatial resolutions for quantitatively accurate estimation of the Chl-a, as the high variation in the phytoplankton biomass happens at smaller than 30 m scales.

The results of S2MCI have potential to improve with an advanced atmospheric correction. Inland waters have the limitation of enhanced atmospheric correction algorithms (discussed in Chapter-2) compared to the ocean water. Toming. [126] used Sen2cor in the Sentinel-2 toolbox for atmospheric correction of Sentinel-2 Level-1 data in mapping Chl-a. However, their results showed a lower correlation of algorithm values versus field measurements. Retrieving the scattering peak around the red-edge region while applying the developed atmospheric corrections has shown ineffective results spatially in the blue-green bloom observations. Sentinel-3 OLCI images were atmospherically corrected using the Case-2 Regional/Coast Colour (C2RCC) tool in SNAP Sentinel-3 toolbox to measure the MCI during the algae bloom. The comparison of TOA radiance and BOA reflectance showed poor performance of C2RCC in the bloom condition [128]. Nevertheless, the red-edge band algorithms are relatively less influenced by the atmospheric effects which is a greater advantage of using this spectral region compared to blue-green algorithms that use the blue green region.

MERISMCI and S2MCI calibration and assessment of performance are presented in Table 3.12 for Chl-a estimation in western Lake Erie, with the statistical performance estimators. We also plotted the estimated Chl-a values of Sentinel-2 and Sentinel-3 retrieval

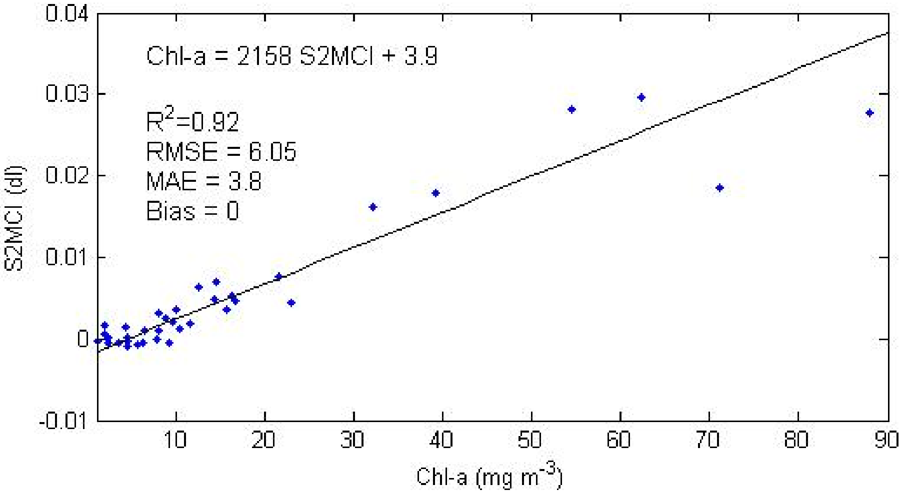

Figure 3.16: Correlation between S2MCI and in-situ Chl-a.

Table 3.12: Performance of the calibration and validation algorithms.

Algorithm	Calibration				Validation			
	R^2	RMSE	MAE	Bias	R^2	RMSE	MAE	Bias
MERISMCI Rad.	0.83	8.59	6.64	0	0.86	8.61	6.01	-1.25
S2MCI Ref.	0.92	6.03	3.8	0	0.84	9.6	6.66	0.15

MCI correlated with the Chl-a measured values to see the 1:1 model estimation performances. We split the extreme data and show the remaining data in the plots desplaing in Figure 3.17. Results indicate no significant differences between the retrieval algorithms in comparison with the in situ measurements, Sentinel-2 ($R^2 = 0.90, 0.84$, $RMSE = 6.03, 9.6$) and Sentinel-3 ($R^2 = 0.83, 0.86$, $RMSE = 8.59, 8.61$) for calibration and validation, respectively. However, inaccurate estimation will be inevitable using all Chl-a concentration ranges affected by deviating the peak along with Chl-a content variation [122].

In this lake study, the result for Sentinel-2 MCI shows better performance ($R^2 = 0.90$). This finding is highly related to the 300 m spatial resolution of OLCI pixel values, it one of the significant problems of ocean satellite application to lake studies with substantial optical property variations in meter scales. Both instrument applications will benefit from

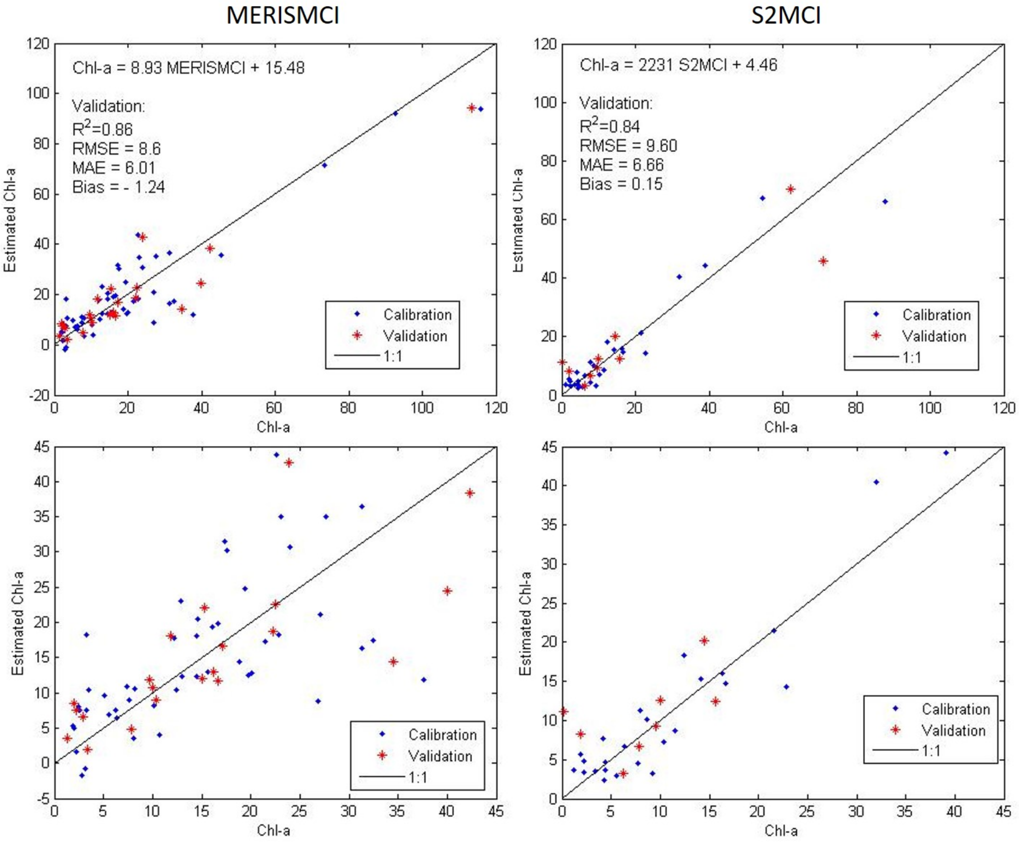

Figure 3.17: Estimated Chl-a vs in situ Chl-a, calibration and validation dataset.

an advanced atmospheric correction.

The MCI has been shown to be negligibly affected by the CDOM due to the spectral distance of red-edge peak from the blue wavelength. In Lake Erie, that the suspended sediment is a major contribution to the optical signal, increasing the magnitude of spectral reflectance, likely is the significant source of error in MCI approaches [122]. The use of MCI in shallow waters may be affected by the seagrasses and sandy bottom which contribute peak reflectances in the red-edge region [129]. To have a more accurate evaluation, we needed more in-situ parameter measurements with fuller information about their quality, and accuracy of measuring instruments in field and laboratory since these highly affect satellite product performances and evaluation.

3.7 Conclusion

This research aimed to evaluate the performance of Sentinel-3 OLCI and Sentinel-2 MSI Chl-a retrieval algorithms in eutrophic lakes using in situ data. We assessed four Chl-a retrieval products. For two of the products (MERISFLH and MERISMCI) already characterized to fit MERIS bands, we configured a new algorithm (S3MCI) based on Sentinel-3 band combination and Sentinel-2 S2MCI product to retrieve Chl-a concentration. We used the Chl-a data from western Lake Erie weekly monitoring stations. The result indicates that the applahn2012developmenticability of FLH is limited to Chl-a range less than 8 $mg\ m^{-3}$. In contrast, the MCI approach is limited to Chl-a retrieval above 20 $mg\ m^{-3}$. However, FLH and MCI approaches both have the advantages of being less influenced by atmospheric effects. Sentinel-2 MCI product offered the highest performance in this study. This performance is mainly related to the high spatial resolution of the MSI sensor which is a necessity of sensor characterization in Chl-a estimation. Furthermore, the performance is due to the maximum peak location of 705 nm in S2MCI band combination compared to 709 nm of MERISMCI signal band position. This study indicates the suitability of Sentinel-3 and Sentinel-2 satellite products using the red-edge scattering approaches for use in monitoring phytoplankton biomass (in large Chl-a range values) with a highly promising result to add services aimed at reducing the impact of the eutrophication on aquatic systems.

3.7.1 Future Work

This research demonstrates the potential of the MCI algorithms to qualitatively monitor green algae blooms in eutrophic lakes . However, there is still some inconsistency between in situ Chl-a measurements and MCI that currently preclude their application as a robust quantitative approach for estimating the bloom condition. This is mainly due to the high variability of regional and temporal optical properties of the water bodies. moreover, diverse phytoplankton taxonomy with different pigment composition, cell size, population distribution, and the display of specific behaviors in different environment conditions particularly in the case of cyanobacteria, which highly impacts on the spectral reflectance due to their vertical distribution in the water column [81]. Therefore, considering variable IOPs in developing bloom monitoring algorithms in addition to considering the depth of phytoplankton in situ sampling for model assessment would enhance bloom studies. This study would be improved by creating Chl-a mapping by the different processors, which could help show the performance of each product in desplaying the extent of a bloom and information about the spatial distribution of Chl-a concentrations.

References

[1] A. N. Tyler, P. D. Hunter, E. Spyrakos, S. Groom, A. M. Constantinescu, and J. Kitchen, “Developments in earth observation for the assessment and monitoring of inland, transitional, coastal and shelf-sea waters,” *Science of The Total Environment*, 2016.

[2] “Us environmental protection agency.” `https://www.epa.gov/greatlakes/lake-erie`.

[3] M. Charlton, J. Vincent, C. Marvin, and J. Ciborowski, “Status of nutrients in the lake erie basin,” *US EPA, Lake Erie*, 2008.

[4] “European space agency website.”

[5] “Fundamental of environmental measurement website.”

[6] R. G. Wetzel, *Limnology: lake and river ecosystems.* Gulf Professional Publishing, 2001.

[7] R. P. Stumpf, L. T. Johnson, T. T. Wynne, and D. B. Baker, “Forecasting annual cyanobacterial bloom biomass to inform management decisions in lake erie,” *Journal of Great Lakes Research*, 2016.

[8] D. Odermatt, A. Gitelson, V. E. Brando, and M. Schaepman, “Review of constituent retrieval in optically deep and complex waters from satellite imagery,” *Remote sensing of environment*, vol. 118, pp. 116–126, 2012.

[9] A. Gilerson, J. Zhou, S. Hlaing, I. Ioannou, B. Gross, F. Moshary, and S. Ahmed, “Fluorescence component in the reflectance spectra from coastal waters. ii. performance of retrieval algorithms,” *Optics express*, vol. 16, no. 4, pp. 2446–2460, 2008.

[10] “Esa earth observation data.” `https://sentinels.copernicus.eu`.

[11] “Us environmental protection agency.” `https://www3.epa.gov/`.

[12] A. Oberemm, J. Becker, G. Codd, and C. Steinberg, “Effects of cyanobacterial toxins and aqueous crude extracts of cyanobacteria on the development of fish and amphibians,” *Environmental Toxicology*, vol. 14, no. 1, pp. 77–88, 1999.

[13] I. Chorus and J. Bartram, “Toxic cyanobacteria in water: a guide to public health significance,” *Monitoring and Management, E & FN Spon, London*, 1999.

[14] J. L. Graham, K. A. Loftin, and N. Kamman, “Monitoring recreational freshwaters,” *Lakelines*, vol. 29, pp. 18–24, 2009.

[15] G. H. Morel, A., “Report of the working group on water color. bound.-layer meteor,” tech. rep., 18 (4), 343-355, 1980.

[16] H. Gordon, O. Brown, R. Evans, J. Brown, R. Smith, and K. Baker, “Semianalytic radiance model of ocean color,” *J. Geophys Res. 93, 10909-10924*, 1988.

[17] N. G. Jerlov, *Marine optics*, vol. 14. Elsevier, 1976.

[18] A. Morel and L. Prieur, “Analysis of variations in ocean color,” *Limnology and oceanography*, vol. 22, no. 4, pp. 709–722, 1977.

[19] H. R. Gordon and A. Y. Morel, *Remote assessment of ocean color for interpretation of satellite visible imagery: a review*, vol. 4. Springer Science & Business Media, 2012.

[20] C. D. Mobley, “The optical properties of water,” *Handbook of optics*, vol. 1, pp. 43–41, 1995.

[21] E. Devred, K. R. Turpie, W. Moses, V. V. Klemas, T. Moisan, M. Babin, G. Toro-Farmer, M.-H. Forget, and Y.-H. Jo, “Future retrievals of water column bio-optical properties using the hyperspectral infrared imager (hyspiri),” *Remote Sensing*, vol. 5, no. 12, pp. 6812–6837, 2013.

[22] T. Kutser, A. Herlevi, K. Kallio, and H. Arst, “A hyperspectral model for interpretation of passive optical remote sensing data from turbid lakes,” *Science of the Total Environment*, vol. 268, no. 1-3, pp. 47–58, 2001.

[23] L. G. Olmanson, P. L. Brezonik, and M. E. Bauer, “Remote sensing for regional lake water quality assessment: capabilities and limitations of current and upcoming satellite systems,” in *Advances in Watershed Science and Assessment*, pp. 111–140, Springer, 2015.

[24] M. W. Matthews, “A current review of empirical procedures of remote sensing in inland and near-coastal transitional waters,” *International Journal of Remote Sensing*, vol. 32, no. 21, pp. 6855–6899, 2011.

[25] H. R. Gordon, O. B. Brown, and M. M. Jacobs, “Computed relationships between the inherent and apparent optical properties of a flat homogeneous ocean,” *Applied optics*, vol. 14, no. 2, pp. 417–427, 1975.

[26] D. Stramski, A. Bricaud, and A. Morel, “Modeling the inherent optical properties of the ocean based on the detailed composition of the planktonic community,” *Applied Optics*, vol. 40, no. 18, pp. 2929–2945, 2001.

[27] C. D. Mobley and L. Sundman, “Hydrolight 4.2,” *Users Guide, Sequoia Scientific, Redmond*, p. 87, 2001.

[28] I. Ogashawara, “Terminology and classification of bio-optical algorithms,” *Remote Sensing Letters*, vol. 6, no. 8, pp. 613–617, 2015.

[29] L. G. Olmanson, P. L. Brezonik, and M. E. Bauer, “Evaluation of medium to low resolution satellite imagery for regional lake water quality assessments,” *Water Resources Research*, vol. 47, no. 9, 2011.

[30] Z. Lee, K. L. Carder, and R. A. Arnone, “Deriving inherent optical properties from water color: a multiband quasi-analytical algorithm for optically deep waters,” *Applied optics*, vol. 41, no. 27, pp. 5755–5772, 2002.

[31] A. Bricaud, M. Babin, A. Morel, and H. Claustre, “Variability in the chlorophyll-specific absorption coefficients of natural phytoplankton: Analysis and parameterization,” *Journal of Geophysical Research: Oceans*, vol. 100, no. C7, pp. 13321–13332, 1995.

[32] L. Li, L. Li, K. Song, Y. Li, L. P. Tedesco, K. Shi, and Z. Li, “An inversion model for deriving inherent optical properties of inland waters: Establishment, validation and application,” *Remote Sensing of Environment*, vol. 135, pp. 150–166, 2013.

[33] A. Morel and F. Villefranche-sur mer, *Bio-optical models.* Academic Press, 2001.

[34] S. M. Kloiber, P. L. Brezonik, L. G. Olmanson, and M. E. Bauer, “A procedure for regional lake water clarity assessment using landsat multispectral data,” *Remote sensing of Environment*, vol. 82, no. 1, pp. 38–47, 2002.

[35] A. A. Gitelson, Y. Gritz, and M. N. Merzlyak, “Relationships between leaf chlorophyll content and spectral reflectance and algorithms for non-destructive chlorophyll assessment in higher plant leaves,” *Journal of plant physiology*, vol. 160, no. 3, pp. 271–282, 2003.

[36] S. G. Simis, A. Ruiz-Verdú, J. A. Domínguez-Gómez, R. Peña-Martinez, S. W. Peters, and H. J. Gons, “Influence of phytoplankton pigment composition on remote sensing of cyanobacterial biomass,” *Remote Sensing of Environment*, vol. 106, no. 4, pp. 414–427, 2007.

[37] A. Bricaud, H. Claustre, J. Ras, and K. Oubelkheir, “Natural variability of phytoplanktonic absorption in oceanic waters: Influence of the size structure of algal populations,” *Journal of Geophysical Research: Oceans*, vol. 109, no. C11, 2004.

[38] J. Kirk, “A theoretical analysis of the contribution of algal cells to the attenuation of light within natural waters ii. spherical cells,” *New Phytologist*, vol. 75, no. 1, pp. 21–36, 1975.

[39] A. A. Gitelson, J. F. Schalles, D. C. Rundquist, F. R. Schiebe, and Y. Z. Yacobi, “Comparative reflectance properties of algal cultures with manipulated densities,” *Journal of Applied Phycology*, vol. 11, no. 4, pp. 345–354, 1999.

[40] K. L. Carder, F. Chen, Z. Lee, S. Hawes, and D. Kamykowski, “Semianalytic moderate-resolution imaging spectrometer algorithms for chlorophyll a and absorption with bio-optical domains based on nitrate-depletion temperatures,” *Journal of Geophysical Research: Oceans*, vol. 104, no. C3, pp. 5403–5421, 1999.

[41] G. Johnsen, N. B. Nelson, R. V. Jovine, and B. B. Prezelin, “Chromoprotein-and pigment-dependent modeling of spectral light absorption in two dinoflagellates, prorocentrum minimum and heterocapsa pygmaea,” *Marine Ecology Progress Series*, pp. 245–258, 1994.

[42] D. ANTOINE, “Sentinel-3 optical products and algorithm definition olci level 2 algorithm theoretical basis document ocean colour products in case 1 waters,” *Date: July*, vol. 13, 2010.

[43] M. Babin, D. Stramski, G. M. Ferrari, H. Claustre, A. Bricaud, G. Obolensky, and N. Hoepffner, “Variations in the light absorption coefficients of phytoplankton, nonalgal particles, and dissolved organic matter in coastal waters around europe,” *Journal of Geophysical Research: Oceans*, vol. 108, no. C7, 2003.

[44] M. Salama, A. Dekker, Z. Su, C. Mannaerts, and W. Verhoef, "Deriving inherent optical properties and associated inversion-uncertainties in the dutch lakes," *Hydrology and Earth System Sciences*, vol. 13, no. 7, pp. 1113–1121, 2009.

[45] R. Doerffer and H. Schiller, "The meris case 2 water algorithm," *International Journal of Remote Sensing*, vol. 28, no. 3-4, pp. 517–535, 2007.

[46] B. Matsushita, W. Yang, G. Yu, Y. Oyama, K. Yoshimura, and T. Fukushima, "A hybrid algorithm for estimating the chlorophyll-a concentration across different trophic states in asian inland waters," *ISPRS journal of photogrammetry and remote sensing*, vol. 102, pp. 28–37, 2015.

[47] D. J. Suggett, O. Prášil, and M. A. Borowitzka, *Chlorophyll a fluorescence in aquatic sciences: methods and applications*. Springer, 2010.

[48] G. Johnsen and E. Sakshaug, "Biooptical characteristics of psii and psi in 33 species (13 pigment groups) of marine phytoplankton, and the relevance for pulse-amplitude-modulated and fast-repetition-rate fluorometry," *Journal of Phycology*, vol. 43, no. 6, pp. 1236–1251, 2007.

[49] O. Schofield, B. Prézelin, and G. Johnsen, "Wavelength dependency of the maximum quantum yield of carbon fixation for two red tide dinoflagellates, heterocapsa pygmaea and prorocentrum minimum (pyrrophyta): Implications for measuring photosynthetic rates," *Journal of phycology*, vol. 32, no. 4, pp. 574–583, 1996.

[50] F. T. Haxo and L. Blinks, "Photosynthetic action spectra of marine algae," *The Journal of general physiology*, vol. 33, no. 4, pp. 389–422, 1950.

[51] H. L. MacIntyre, T. M. Kana, T. Anning, and R. J. Geider, "Photoacclimation of photosynthesis irradiance response curves and photosynthetic pigments in microalgae and cyanobacteria," *Journal of phycology*, vol. 38, no. 1, pp. 17–38, 2002.

[52] I. Sassenhagen, K. Rengefors, T. L. Richardson, and J. L. Pinckney, "Pigment composition and photoacclimation as keys to the ecological success of gonyostomum semen (raphidophyceae, stramenopiles)," *Journal of phycology*, vol. 50, no. 6, pp. 1146–1154, 2014.

[53] K. Lebret, E. S. Kritzberg, and K. Rengefors, "Population genetic structure of a microalgal species under expansion," *PloS one*, vol. 8, no. 12, p. e82510, 2013.

[54] C. Trigal, S. Hallstan, K. S. Johansson, and R. K. Johnson, “Factors affecting occurrence and bloom formation of the nuisance flagellate gonyostomum semen in boreal lakes,” *Harmful algae*, vol. 27, pp. 60–67, 2013.

[55] M. Olin, M. Rask, J. Ruuhijärvi, J. Keskitalo, J. Horppila, P. Tallberg, T. Taponen, A. Lehtovaara, and I. Sammalkorpi, “Effects of biomanipulation on fish and plankton communities in ten eutrophic lakes of southern finland,” *Hydrobiologia*, vol. 553, no. 1, pp. 67–88, 2006.

[56] K. S. Johansson, T. Vrede, K. Lebret, and R. K. Johnson, “Zooplankton feeding on the nuisance flagellate gonyostomum semen,” *PloS one*, vol. 8, no. 5, p. e62557, 2013.

[57] D. Findlay, J. Paterson, L. Hendzel, and H. Kling, “Factors influencing gonyostomum semen blooms in a small boreal reservoir lake,” *Hydrobiologia*, vol. 533, no. 1-3, pp. 243–252, 2005.

[58] K. Salonen and M. Rosenberg, “Advantages from diel vertical migration can explain the dominance of gonyostomum semen (raphidophyceae) in a small, steeply-stratified humic lake,” *Journal of Plankton Research*, vol. 22, no. 10, pp. 1841–1853, 2000.

[59] M. Wyman and P. Fay, “Underwater light climate and the growth and pigmentation of planktonic blue-green algae (cyanobacteria) i. the influence of light quantity,” *Proc. R. Soc. Lond. B*, vol. 227, no. 1248, pp. 367–380, 1986.

[60] G. Johnsen, B. B. Prézelin, and R. V. Jovine, “Fluorescence excitation spectra and light utilization in two red tide dinoflagellates,” *Limnology and Oceanography*, vol. 42, no. 5part2, pp. 1166–1177, 1997.

[61] S. G. Simis, Y. Huot, M. Babin, J. Seppälä, and L. Metsamaa, “Optimization of variable fluorescence measurements of phytoplankton communities with cyanobacteria,” *Photosynthesis research*, vol. 112, no. 1, pp. 13–30, 2012.

[62] M. W. Matthews, S. Bernard, and L. Robertson, “An algorithm for detecting trophic status (chlorophyll-a), cyanobacterial-dominance, surface scums and floating vegetation in inland and coastal waters,” *Remote Sensing of Environment*, vol. 124, pp. 637–652, 2012.

[63] T. Wynne, R. Stumpf, M. Tomlinson, R. Warner, P. Tester, J. Dyble, and G. Fahnenstiel, “Relating spectral shape to cyanobacterial blooms in the laurentian great lakes,” *International Journal of Remote Sensing*, vol. 29, no. 12, pp. 3665–3672, 2008.

[64] Y. Huot and M. Babin, "Overview of fluorescence protocols: theory, basic concepts, and practice," in *Chlorophyll a fluorescence in aquatic sciences: Methods and applications*, pp. 31–74, Springer, 2010.

[65] J. Gower, R. Doerffer, and G. Borstad, "Interpretation of the 685nm peak in water-leaving radiance spectra in terms of fluorescence, absorption and scattering, and its observation by meris," *International Journal of Remote Sensing*, vol. 20, no. 9, pp. 1771–1786, 1999.

[66] J. Fischer and U. Kronfeld, "Sun-stimulated chlorophyll fluorescence 1: Influence of oceanic properties," *TitleREMOTE SENSING*, vol. 11, no. 12, pp. 2125–2147, 1990.

[67] D. McKee, A. Cunningham, D. Wright, and L. Hay, "Potential impacts of nonalgal materials on water-leaving sun induced chlorophyll fluorescence signals in coastal waters," *Applied optics*, vol. 46, no. 31, pp. 7720–7729, 2007.

[68] B. Tao, Z. Mao, D. Pan, Y. Shen, Q. Zhu, and J. Chen, "Influence of bio-optical parameter variability on the reflectance peak position in the red band of algal bloom waters," *Ecological informatics*, vol. 16, pp. 17–24, 2013.

[69] R. M. Letelier and M. R. Abbott, "An analysis of chlorophyll fluorescence algorithms for the moderate resolution imaging spectrometer (modis)," *Remote Sensing of Environment*, vol. 58, no. 2, pp. 215–223, 1996.

[70] A. Gitelson, "The peak near 700 nm on radiance spectra of algae and water: relationships of its magnitude and position with chlorophyll concentration," *International Journal of Remote Sensing*, vol. 13, no. 17, pp. 3367–3373, 1992.

[71] J. F. Schalles, A. A. Gitelson, Y. Z. Yacobi, and A. E. Kroenke, "Estimation of chlorophyll a from time series measurements of high spectral resolution reflectance in an eutrophic lake," *Journal of Phycology*, vol. 34, no. 2, pp. 383–390, 1998.

[72] M. W. Matthews and D. Odermatt, "Improved algorithm for routine monitoring of cyanobacteria and eutrophication in inland and near-coastal waters," *Remote Sensing of Environment*, vol. 156, pp. 374–382, 2015.

[73] S. C. Palmer, V. V. Pelevin, I. Goncharenko, A. W. Kovács, A. Zlinszky, M. Présing, H. Horváth, V. Nicolás-Perea, H. Balzter, and V. R. Tóth, "Ultraviolet fluorescence lidar (ufl) as a measurement tool for water quality parameters in turbid lake conditions," *Remote Sensing*, vol. 5, no. 9, pp. 4405–4422, 2013.

[74] R. Neville and J. Gower, “Passive remote sensing of phytoplankton via chlorophyll α fluorescence,” *Journal of Geophysical Research*, vol. 82, no. 24, pp. 3487–3493, 1977.

[75] C. F. Bohren and D. R. Huffman, *Absorption and scattering by a sphere.* Wiley Online Library, 1983.

[76] M. Hieronymi, A. Macke, and O. Zielinski, “Modeling of wave-induced irradiance variability in the upper ocean mixed layer,” *Ocean Science*, vol. 8, no. 2, pp. 103–120, 2012.

[77] W. Zhou, G. Wang, Z. Sun, W. Cao, Z. Xu, S. Hu, and J. Zhao, “Variations in the optical scattering properties of phytoplankton cultures,” *Optics Express*, vol. 20, no. 10, pp. 11189–11206, 2012.

[78] M. Quinby-Hunt, A. Hunt, K. Lofftus, and D. Shapiro, “Polarized-light scattering studies of marine chlorella,” *Limnology and oceanography*, vol. 34, no. 8, pp. 1587–1600, 1989.

[79] H. Volten, J. De Haan, J. Hovenier, R. Schreurs, W. Vassen, A. Dekker, H. Hoogenboom, F. Charlton, and R. Wouts, “Laboratory measurements of angular distributions of light scattered by phytoplankton and silt,” *Limnology and oceanography*, vol. 43, no. 6, pp. 1180–1197, 1998.

[80] C. Dupouy, J. Neveux, G. Dirberg, R. Rottgers, M. Tenório, and S. Ouillon, “Bio-optical properties of the marine cyanobacteria trichodesmium spp.,” *Journal of Applied Remote Sensing*, vol. 2, no. 1, p. 023503, 2008.

[81] T. Kutser, L. Metsamaa, and A. G. Dekker, “Influence of the vertical distribution of cyanobacteria in the water column on the remote sensing signal,” *Estuarine, Coastal and Shelf Science*, vol. 78, no. 4, pp. 649–654, 2008.

[82] R. D. Vaillancourt, C. W. Brown, R. R. Guillard, and W. M. Balch, “Light backscattering properties of marine phytoplankton: relationships to cell size, chemical composition and taxonomy,” *Journal of plankton research*, vol. 26, no. 2, pp. 191–212, 2004.

[83] A. L. Whitmire, W. S. Pegau, L. Karp-Boss, E. Boss, and T. J. Cowles, “Spectral backscattering properties of marine phytoplankton cultures,” *Optics Express*, vol. 18, no. 14, pp. 15073–15093, 2010.

[84] G. Quibell, "Estimating chlorophyll concentrations using upwelling radiance from different freshwater algal genera," *International Journal of Remote Sensing*, vol. 13, no. 14, pp. 2611–2621, 1992.

[85] Y. Huot, M. Babin, F. Bruyant, C. Grob, M. Twardowski, and H. Claustre, "Does chlorophyll a provide the best index of phytoplankton biomass for primary productivity studies," *Biogeosciences discussions*, vol. 4, no. 2, pp. 707–745, 2007.

[86] C. Le, Y. Li, Y. Zha, D. Sun, C. Huang, and H. Lu, "A four-band semi-analytical model for estimating chlorophyll a in highly turbid lakes: The case of taihu lake, china," *Remote Sensing of Environment*, vol. 113, no. 6, pp. 1175–1182, 2009.

[87] S. Mishra and D. R. Mishra, "Normalized difference chlorophyll index: A novel model for remote estimation of chlorophyll-a concentration in turbid productive waters," *Remote Sensing of Environment*, vol. 117, pp. 394–406, 2012.

[88] F. E. Dierberg and N. E. Carriker, "Field testing two instruments for remotely sensing water quality in the tennessee valley," *Environmental science & technology*, vol. 28, no. 1, pp. 16–25, 1994.

[89] Y. Z. Yacobi, A. Gitelson, and M. Mayo, "Remote sensing of chlorophyll in lake kinneret using highspectral-resolution radiometer and landsat tm: spectral features of reflectance and algorithm development," *Journal of Plankton Research*, vol. 17, no. 11, pp. 2155–2173, 1995.

[90] J. Gower, S. King, G. Borstad, and L. Brown, "Detection of intense plankton blooms using the 709 nm band of the meris imaging spectrometer," *International Journal of Remote Sensing*, vol. 26, no. 9, pp. 2005–2012, 2005.

[91] J. P. Ryan, C. O. Davis, N. B. Tufillaro, R. M. Kudela, and B.-C. Gao, "Application of the hyperspectral imager for the coastal ocean to phytoplankton ecology studies in monterey bay, ca, usa," *Remote Sensing*, vol. 6, no. 2, pp. 1007–1025, 2014.

[92] M. W. Matthews and S. Bernard, "Characterizing the absorption properties for remote sensing of three small optically-diverse south african reservoirs," *Remote Sensing*, vol. 5, no. 9, pp. 4370–4404, 2013.

[93] K.-H. Mittenzwey, S. Ullrich, A. Gitelson, and K. Kondratiev, "Determination of chlorophyll a of inland waters on the basis of spectral reflectance," *Limnology and Oceanography*, vol. 37, no. 1, pp. 147–149, 1992.

[94] J. Gower, S. King, and P. Goncalves, "Global monitoring of plankton blooms using meris mci," *International Journal of Remote Sensing*, vol. 29, no. 21, pp. 6209–6216, 2008.

[95] T. T. Wynne, R. P. Stumpf, M. C. Tomlinson, and J. Dyble, "Characterizing a cyanobacterial bloom in western lake erie using satellite imagery and meteorological data," *Limnology and Oceanography*, vol. 55, no. 5, pp. 2025–2036, 2010.

[96] D. Blondeau-Patissier, J. F. Gower, A. G. Dekker, S. R. Phinn, and V. E. Brando, "A review of ocean color remote sensing methods and statistical techniques for the detection, mapping and analysis of phytoplankton blooms in coastal and open oceans," *Progress in oceanography*, vol. 123, pp. 123–144, 2014.

[97] J. W. Campbell and H. Feng, "The empirical chlorophyll algorithm for modis: Testing the oc3m algorithm using nomad data," in *Ocean Color Bio-optical Algorithm Mini-workshop*, pp. 27–29, 2005.

[98] J. E. O'Reilly, S. Maritorena, B. G. Mitchell, D. A. Siegel, K. L. Carder, S. A. Garver, M. Kahru, and C. McClain, "Ocean color chlorophyll algorithms for seawifs," *Journal of Geophysical Research: Oceans*, vol. 103, no. C11, pp. 24937–24953, 1998.

[99] C. Hu, F. E. Muller-Karger, C. J. Taylor, K. L. Carder, C. Kelble, E. Johns, and C. A. Heil, "Red tide detection and tracing using modis fluorescence data: A regional example in sw florida coastal waters," *Remote Sensing of Environment*, vol. 97, no. 3, pp. 311–321, 2005.

[100] J. Gower, S. King, W. Yan, G. Borstad, and L. Brown, "Use of the 709 nm band of meris to detect intense plankton blooms and other conditions in coastal waters," in *Proc. MERIS User Workshop, Frascati, Italy, 10–13 November 2003*, Citeseer, 2003.

[101] C. Hu, "A novel ocean color index to detect floating algae in the global oceans," *Remote Sensing of Environment*, vol. 113, no. 10, pp. 2118–2129, 2009.

[102] C. Hu, Z. Lee, and B. Franz, "Chlorophyll aalgorithms for oligotrophic oceans: A novel approach based on three-band reflectance difference," *Journal of Geophysical Research: Oceans*, vol. 117, no. C1, 2012.

[103] R. J. Brewin, D. E. Raitsos, Y. Pradhan, and I. Hoteit, "Comparison of chlorophyll in the red sea derived from modis-aqua and in vivo fluorescence," *Remote Sensing of Environment*, vol. 136, pp. 218–224, 2013.

[104] A. G. Dekker, “Detection of optical water quality parameters for eutrophic waters by high resolution remote sensing,” 1993.

[105] E. Tebbs, J. Remedios, and D. Harper, “Remote sensing of chlorophyll-a as a measure of cyanobacterial biomass in lake bogoria, a hypertrophic, saline–alkaline, flamingo lake, using landsat etm+,” *Remote Sensing of Environment*, vol. 135, pp. 92–106, 2013.

[106] L. G. Olmanson, M. E. Bauer, and P. L. Brezonik, “A 20-year landsat water clarity census of minnesota’s 10,000 lakes,” *Remote Sensing of Environment*, vol. 112, no. 11, pp. 4086–4097, 2008.

[107] T. Kutser, D. C. Pierson, K. Y. Kallio, A. Reinart, and S. Sobek, “Mapping lake cdom by satellite remote sensing,” *Remote Sensing of Environment*, vol. 94, no. 4, pp. 535–540, 2005.

[108] S. Pal, I. Gregory-Eaves, and F. Pick, “Temporal trends in cyanobacteria revealed through dna and pigment analyses of temperate lake sediment cores,” *Journal of Paleolimnology*, vol. 54, no. 1, pp. 87–101, 2015.

[109] C. Mortimer, “Discoveries and testable hypotheses arising from coastal zone color scanner imagery of southern lake michigan,” *Limnology and Oceanography*, vol. 33, no. 2, pp. 203–226, 1988.

[110] D. L. Witter, J. D. Ortiz, S. Palm, R. T. Heath, and J. W. Budd, “Assessing the application of seawifs ocean color algorithms to lake erie,” *Journal of Great Lakes Research*, vol. 35, no. 3, pp. 361–370, 2009.

[111] M. Wang and W. Shi, “The nir-swir combined atmospheric correction approach for modis ocean color data processing,” *Optics Express*, vol. 15, no. 24, pp. 15722–15733, 2007.

[112] S. C. Palmer, T. Kutser, and P. D. Hunter, “Remote sensing of inland waters: Challenges, progress and future directions,” *Remote Sensing of Environment*, vol. 157, pp. 1–8, 2015.

[113] G. S. Fargion and J. L. Mueller, *Ocean optics protocols for satellite ocean color sensor validation, Revision 2.* National Aeronautics and Space Administration, Goddard Space Flight Center, 2000.

[114] A. Daghighi, "Harmful algae bloom prediction model for western lake erie using stepwise multiple regression and genetic programming," 2017.

[115] A. Daghighi, A. Nahvi, and U. Kim, "Optimal cultivation pattern to increase revenue and reduce water use: Application of linear programming to arjan plain in fars province," *Agriculture*, vol. 7, no. 9, p. 73, 2017.

[116] M. J. Maccoux, A. Dove, S. M. Backus, and D. M. Dolan, "Total and soluble reactive phosphorus loadings to lake erie: A detailed accounting by year, basin, country, and tributary," *Journal of Great Lakes Research*, vol. 42, no. 6, pp. 1151–1165, 2016.

[117] L. E. Allinger and E. D. Reavie, "The ecological history of lake erie as recorded by the phytoplankton community," *Journal of Great Lakes Research*, vol. 39, no. 3, pp. 365–382, 2013.

[118] A. M. Michalak, E. J. Anderson, D. Beletsky, S. Boland, N. S. Bosch, T. B. Bridgeman, J. D. Chaffin, K. Cho, R. Confesor, I. Daloğlu, *et al.*, "Record-setting algal bloom in lake erie caused by agricultural and meteorological trends consistent with expected future conditions," *Proceedings of the National Academy of Sciences*, vol. 110, no. 16, pp. 6448–6452, 2013.

[119] "Noaa - great lakes environmental research laboratory." `https://www.greatersudbury.ca/`.

[120] C. Binding, T. Greenberg, and R. Bukata, "The meris maximum chlorophyll index; its merits and limitations for inland water algal bloom monitoring," *Journal of Great Lakes Research*, vol. 39, pp. 100–107, 2013.

[121] T. Wynne, R. Stumpf, and T. Briggs, "Comparing modis and meris spectral shapes for cyanobacterial bloom detection," *International journal of remote sensing*, vol. 34, no. 19, pp. 6668–6678, 2013.

[122] P. B. Augusto-Silva, I. Ogashawara, C. C. Barbosa, L. A. De Carvalho, D. S. Jorge, C. I. Fornari, and J. L. Stech, "Analysis of meris reflectance algorithms for estimating chlorophyll-a concentration in a brazilian reservoir," *Remote Sensing*, vol. 6, no. 12, pp. 11689–11707, 2014.

[123] A. A. Gitelson, D. Gurlin, W. J. Moses, and T. Barrow, "A bio-optical algorithm for the remote estimation of the chlorophyll-a concentration in case 2 waters," *Environmental Research Letters*, vol. 4, no. 4, p. 045003, 2009.

[124] C. Binding, T. Greenberg, J. Jerome, R. Bukata, and G. Letourneau, “An assessment of meris algal products during an intense bloom in lake of the woods,” *Journal of Plankton Research*, vol. 33, no. 5, pp. 793–806, 2010.

[125] W. J. Moses, A. A. Gitelson, S. Berdnikov, and V. Povazhnyy, “Satellite estimation of chlorophyll-*a* concentration using the red and nir bands of meristhe azov sea case study,” *IEEE Geoscience and Remote Sensing Letters*, vol. 6, no. 4, pp. 845–849, 2009.

[126] K. Toming, T. Kutser, A. Laas, M. Sepp, B. Paavel, and T. Nõges, “First experiences in mapping lake water quality parameters with sentinel-2 msi imagery,” *Remote Sensing*, vol. 8, no. 8, p. 640, 2016.

[127] T. Kutser, “Quantitative detection of chlorophyll in cyanobacterial blooms by satellite remote sensing,” *Limnology and Oceanography*, vol. 49, no. 6, pp. 2179–2189, 2004.

[128] K. Toming, T. Kutser, R. Uiboupin, A. Arikas, K. Vahter, and B. Paavel, “Mapping water quality parameters with sentinel-3 ocean and land colour instrument imagery in the baltic sea,” *Remote Sensing*, vol. 9, no. 10, p. 1070, 2017.

[129] V. J. Hill, R. C. Zimmerman, W. P. Bissett, H. Dierssen, and D. D. Kohler, “Evaluating light availability, seagrass biomass, and productivity using hyperspectral airborne remote sensing in saint josephs bay, florida,” *Estuaries and coasts*, vol. 37, no. 6, pp. 1467–1489, 2014.